Journal of Geophysical Research: Atmospheres

RESEARCH ARTICLE
10.1029/2017JD026889

Special Section:
The Arctic: An AGU Joint Special Collection

Link Between Arctic Tropospheric BrO Explosion Observed From Space and Sea-Salt Aerosols From Blowing Snow Investigated Using Ozone Monitoring Instrument BrO Data and GEOS-5 Data Assimilation System

S. Choi[1,2], N. Theys[3], R. J. Salawitch[4,5,6], P. A. Wales[4], J. Joiner[2], T. P. Canty[4], K. Chance[7], R. M. Suleiman[7], S. P. Palm[1,2], R. I. Cullather[2,4], A. S. Darmenov[2], A. da Silva[2], T. P. Kurosu[8], F. Hendrick[3], and M. Van Roozendael[3]

[1]Science Systems and Applications, Inc., Lanham, MD, USA, [2]NASA Goddard Space Flight Center, Greenbelt, MD, USA, [3]Belgian Institute for Space Aeronomy (BIRA-IASB), Brussels, Belgium, [4]Department of Atmospheric and Oceanic Science, University of Maryland, College Park, MD, USA, [5]Earth System Science Interdisciplinary Center, University of Maryland, College Park, MD, USA, [6]Department of Chemistry and Biochemistry, University of Maryland, College Park, MD, USA, [7]Harvard-Smithsonian Center for Astrophysics, Cambridge, MA, USA, [8]NASA Jet Propulsion Laboratory/California Institute of Technology, Pasadena, CA, USA

Key Points:
- OMI-observed Arctic tropospheric BrO explosions are associated with GEOS-5 simulated sea-salt aerosols (SSAs) from wind-driven blowing snow
- The 11-year time series analysis shows that the Arctic BrO explosion frequency and simulated blowing snow SSA emission flux are correlated
- The satellite-based record of first-year sea ice area does not show significant correlation with the Arctic BrO explosion frequency

Supporting Information:
- Supporting Information S1

Correspondence to:
S. Choi,
sungyeon.choi@nasa.gov

Citation:
Choi, S., Theys, N., Salawitch, R. J., Wales, P. A., Joiner, J., Canty, T. P., et al. (2018). Link between Arctic tropospheric BrO explosion observed from space and sea-salt aerosols from blowing snow investigated using Ozone Monitoring Instrument BrO data and GEOS-5 data assimilation system. *Journal of Geophysical Research: Atmospheres*, *123*, 6954–6983. https://doi.org/10.1029/2017JD026889

Received 31 MAR 2017
Accepted 28 MAR 2018
Accepted article online 21 MAY 2018
Published online 5 JUL 2018

Abstract Bromine radicals (Br + BrO) are important atmospheric species owing to their ability to catalytically destroy ozone as well as their potential impacts on the oxidative pathways of many trace gases, including dimethylsulfide and mercury. Using space-based observations of BrO, recent studies have reported rapid enhancements of tropospheric BrO over large areas (so called "BrO explosions") connected to near-surface ozone depletion occurring in polar spring. However, the source(s) of reactive bromine and mechanism(s) that initiate these BrO explosions are uncertain. In this study, we investigate the relationships between Arctic BrO explosions and two of the proposed sources of reactive bromine: sea-salt aerosol (SSA) generated from blowing snow and first-year (seasonal) sea ice. We use tropospheric column BrO derived from the Ozone Monitoring Instrument (OMI) in conjunction with the Goddard Earth Observing System Version 5 (GEOS-5) data assimilation system provided by National Aeronautics and Space Administration Global Modeling and Assimilation Office. Case studies demonstrate a strong association between the temporal and spatial extent of OMI-observed BrO explosions and the GEOS-5 simulated blowing snow-generated SSA during Arctic spring. Furthermore, the frequency of BrO explosion events observed over the 11-year record of OMI exhibits significant correlation with a time series of the simulated SSA emission flux in the Arctic and little to no correlation with a time series of satellite-based first-year sea ice area. Therefore, we conclude that SSA generated by blowing snow is an important factor in the formation of the BrO explosion observed from space during Arctic spring.

1. Introduction

Bromine radicals (Br and BrO) are important tropospheric trace species owing to their ability to catalytically destroy ozone (O_3) and to alter the oxidation processes of mercury (Ariya et al., 2002) and sulfur species including dimethylsulfide (Toumi, 1994). Bromine chemistry during polar sunrise, in particular, has been of long-term interest to the atmospheric science community; the cause of widespread polar tropospheric ozone depletion events (ODEs) was found to be inorganic bromine species (e.g., Barrie et al., 1988). Although initial investigations of polar bromine chemistry centered around polar tropospheric ODEs, the importance of bromine in the polar environment has been shown to extend into other research areas. For instance, bromine radicals affect polar environments by oxidizing gaseous elemental mercury (Hg^0) to reactive gaseous mercury (Hg^{2+}) that easily deposits into the polar environment (e.g., Ariya et al., 2004; Douglas et al., 2005; Ebinghaus et al., 2002; Lu et al., 2001; Steffen et al., 2013). The sizable quantity of bromine radicals produced in polar regions may also supply inorganic bromine to the subpolar atmosphere. Outside the polar regions, this may potentially alter the concentrations of tropospheric ozone (Parrella et al., 2012; Saiz-Lopez et al., 2012; Yang et al., 2005) as well as the mercury budget (Holmes et al., 2006, 2010; Parrella et al., 2012; Seigneur & Lohman, 2008) and chemical pathways of cloud condensation nuclei (Breider et al., 2010; von Glasow & Crutzen, 2004).

A primary source of bromine radicals in the polar troposphere is thought to be bromide (Br^-, the ionized form of bromine) contained in sea salt. Since Br^- is usually very stable due to the high electron affinity of Br, oxidation of Br^- (i.e., losing an electron) requires a special circumstance. The key process is the acid-catalyzed reaction in a condensed phase that transforms bromide into molecular bromine (Br_2; e.g., Fan & Jacob, 1992:

$$HOBr + Br^- + H^+ \rightarrow H_2O + Br_2(\text{condensed phase}). \quad (1)$$

Br_2 is released to the atmosphere due to its low solubility and is photolyzed to yield the bromine radical (or atomic bromine, Br):

$$Br_2 + h\nu \rightarrow 2Br(\text{gas phase}). \quad (2)$$

The resulting bromine radicals lead to catalytic loss of ozone; that is,

$$Br + O_3 \rightarrow BrO + O_2 \quad (3)$$

$$BrO + XO \rightarrow BrX + O_2 (X = Br, Cl, I, \text{and } OH) \quad (4)$$

$$BrX + h\nu \rightarrow Br + X. \quad (5)$$

The inorganic bromine species containing oxidized bromine (Br, BrO, Br_2, BrCl, BrI, and HOBr) can be considered as "activated" since these species are either radicals or can readily form radicals by photolysis. Products from gas phase reactions may return to the condensed phase for further bromine activation ("recycling") since HOBr is required for oxidation of Br^-. For more details on the chemistry, see Simpson et al. (2007) and Abbatt et al. (2012).

There are two meanings of the term "bromine explosion" in the scientific literature. Wennberg (1999) first used this term to describe the autocatalytic cycle that sharply increases the abundance of bromine monoxide (BrO) upon return of sunlight in the Arctic. Other papers used bromine explosion to refer to the large synoptic-scale enhancements of tropospheric BrO observed during polar spring from space (e.g., Schofield et al., 2006; Van Roozendael et al., 2002). Here we use the term "BrO explosion" to refer to the spaceborne observation of synoptic-scale enhancement of tropospheric BrO. Chance (1998) and Hegels et al. (1998) were the first to show that the springtime enhancement of tropospheric BrO in the Arctic can occur over large geographic regions, such that elevated total column BrO is readily visible from space.

The exact mechanism of the bromine activation remains uncertain. Suggested hypotheses include (and are not mutually exclusive) the following: (1) snowpack over first-year (seasonal) sea ice and coastal regions (Pratt et al., 2013; Toyota et al., 2014); (2) snow particles blown by wind (Jones et al., 2009, 2010; Yang et al., 2008, 2010); (3) first-year sea ice (Jones et al., 2006; Nghiem et al., 2012; Simpson et al., 2007; Wagner et al., 2007); and (4) frost flowers (Kaleschke et al., 2004; Nghiem et al., 2012). Recent laboratory (Wren et al., 2013) and field (Pratt et al., 2013) studies have reported active bromine release from acidic, saline snowpack in the presence of ozone and sunlight. In particular, Pratt et al. (2013) showed that the surface snowpack emits Br_2, while first-year sea ice does not produce Br_2. The HO_x ($OH+HO_2$) and NO_x ($NO+NO_2$) radicals produced from snowpack photochemistry (Jones et al., 2001; Sumner & Shepson, 1999; Zhou et al., 2001) play important roles in the proposed mechanism. In the quasi-brine layer of a snow grain surface, bromide (Br^-) is oxidized by ozonation to form HOBr and transforms to Br_2 (equation (1)) or the OH radical oxidizes Br^- to form Br_2. Molecular bromine, Br_2, is released to the snowpack interstitial air and transforms to BrO in the presence of O_3 and sunlight (equations (2) and (3)). Reactions of BrO with HO_2 and NO_2 produce HOBr and $BrONO_2$, respectively, that recycle into the brine layer to accelerate further bromine activation. Wind pumping into the snowpack is necessary for the supply of O_3 in this mechanism. Burd et al. (2017) reported that the BrO seasonal end date was highly correlated with the snowmelt onset date and that BrO was only observed at temperatures below the freezing point. Peterson et al. (2017) emphasized the role of heterogeneous recycling on aerosol particles that releases labile bromine species as being an important component of the mechanism that results in elevated BrO in the free troposphere.

Studies have suggested two regimes of bromine release from snow depending on the wind speed. At low wind speeds, reactive bromine is released from the wind-pumped sunlit snowpack. However, at high wind speeds, reactive bromine can be released from snow particles blown into the atmosphere (Abbatt et al., 2012; Jones et al., 2009). Depleted bromide (Br^-) relative to chloride (Cl^-) in Antarctic blowing snow particles, as compared with typical sea water composition, supports this hypothesis in the Antarctic (Lieb-Lappen & Obbard, 2015).

BrO has been the most commonly observed of the activated bromine species since it absorbs ultraviolet (UV) radiation and can be detected with remote sensing techniques (e.g., Chance, 1998; Salawitch et al., 2010). A number of BrO measurements that make use of differential optical absorption spectroscopy (DOAS) techniques have been made from various platforms. For example, measurements using the ground-based Long-Pass-DOAS (LP-DOAS) techniques have reported near-surface-enhanced BrO episodes during the polar springtime (Hausmann & Platt, 1994; Hönninger et al., 2004; Martinez et al., 1999; Tuckermann et al., 1997). Pöhler et al. (2010) reported enhanced BrO over first-year sea ice at Amundsen Gulf using an LP-DOAS instrument aboard the Canadian Coast Guard Ship vessel Amundsen during the Ocean Atmospheric Sea Ice Snowpack (OASIS)-Canada campaign. Studies using airborne DOAS instruments have demonstrated the capability to obtain free tropospheric BrO abundances (McElroy et al., 1999; Peterson et al., 2017; Prados-Roman et al., 2011). Analysis of multiple-axis DOAS measurements (Hönninger et al., 2004) has suggested a correlation between BrO abundances and contact with first-year sea ice (Simpson et al., 2007). These multiple-axis DOAS observations also further enable investigation of the vertical distribution of BrO in conjunction with atmospheric stability (Peterson et al., 2015; Simpson et al., 2017).

Space-based, remotely sensed measurements of BrO offer valuable information to study polar tropospheric bromine chemistry, because they can image vast areas that are otherwise difficult to cover with suborbital platforms. Because of the relatively high surface albedo of snow and ice in the polar environment, space-borne UV measurements are more sensitive toward the troposphere than other regions with lower surface albedo (Choi et al., 2012; Theys et al., 2011). Since total column BrO measurements became available from nadir-viewing observations of the Global Ozone Monitoring Experiment (GOME) aboard the European Space Agency European Remote Sensing 2 satellite (Chance, 1998, 2002; Hegels et al., 1998; Richter et al., 1998; Wagner & Platt, 1998), similar approaches have been applied to other UV satellite instruments including the SCanning Image Absorption SpectroMeter for Atmospheric CHartographY on the European Space Agency Environmental Satellite (EnviSat; Theys et al., 2004, the Ozone Monitoring Instrument (OMI) aboard U.S. National Aeronautics and Space Administration (NASA) Aura spacecraft (Choi et al., 2012; Salawitch et al., 2010), and the second GOME on the series of European Organisation for the Exploitation of Meteorological Satellites (MetOp; Begoin et al., 2010; Blechschmidt et al., 2015; Theys et al., 2011; Zhao et al., 2016).

Tropospheric column BrO can be retrieved from nadir-viewing satellite measurements after subtraction of an estimated stratospheric burden (Salawitch et al., 2010; Theys et al., 2009) and radiative transfer analysis. One of the most noticeable findings from the early era of satellite measurements is the rapid increase of tropospheric BrO lasting several days over large areas reported from the early era of satellite BrO measurements (e.g., Chance, 1998; Wagner & Platt, 1998). Beyond the mere reporting of such phenomena, the excellent spatial coverage of large swath satellite instruments allows for the study of the origin and behaviors of tropospheric BrO explosions over the entire Arctic and Antarctic regions. For example, Begoin et al. (2010) investigated a BrO explosion coincident with a polar cyclone and its potential long-range transport using GOME-2 BrO data and the FLEXible PARTicle dispersion model. Blechschmidt et al. (2015) analyzed an enhanced BrO event in context of frontal activities near a low-pressure system using GOME-2 BrO and European Center for Medium range Weather Forecasting meteorological data. Moreover, measurements from polar-orbiting spacecraft allow the evolution of BrO explosions to be traced with fine temporal resolution ($\sim$1.5 hr) owing to frequent overpasses at high latitudes (Choi et al., 2012).

The abundance of BrO can also be observed in situ using chemical ionization mass spectroscopy (CIMS) from ground- and aircraft-based platforms (Buys et al., 2013; Liao, Huey, Scheuer, et al., 2012; Liao, Huey, Tanner, et al., 2012; Liao et al., 2011; Neuman et al., 2010; Peterson et al., 2015). However, such measurements are sparse since they are typically made during a limited number of specialized field campaigns. Comprehensive analysis of aircraft measurements, OMI tropospheric column BrO, and meteorological reanalysis indicated that Arctic tropospheric BrO explosion events can be connected with near-surface weather, including high wind speeds and high planetary boundary layer (PBL) heights (Choi et al., 2012).

There is interest in understanding the role of climate change in the Arctic on BrO explosions as well as ODEs (e.g., Burd et al., 2017; Hollwedel et al., 2004). Tropospheric ODEs do not always coincide with tropospheric BrO enhancements observable by nadir-viewing satellite instruments. We do not expect to see enhanced tropospheric column BrO where O_3 is severely depleted ($\lesssim$1 ppbv), because active bromine (Br+BrO) partitions to atomic Br when ambient levels of O_3 are suppressed (Choi et al., 2012; Simpson et al., 2007). In the Arctic, downward transport of air from the free troposphere to the convectively mixed boundary layer acts

as a source of O_3 to the lowermost atmosphere. This source of O_3 is strongest under conditions of deep mixing and/or strong winds. When the mixed layer is shallow and wind speed is low, O_3 can be quickly depleted to a sub-parts per billion level and active bromine will be present mainly as Br. This may explain why Jones et al. (2009) associate some ODEs (in the Antarctic) with conditions of low wind speed and others with high wind speed based on modeling results, while at the same time they stated that satellite measurements of elevated column BrO were only reported under conditions of high wind speed during October 2007 over the Weddell Sea. The Jones et al. (2009) study does not preclude the presence of elevated BrO mixing ratios existing under conditions of low wind speed and shallow boundary layer.

For a BrO explosion to be observable from a nadir-viewing satellite instrument, either a high boundary layer height (i.e., deep mixing layer) condition is required or the enhanced BrO must extend above the top of the convective boundary layer. Since satellite measurements retrieve tropospheric column BrO, even highly elevated mixing ratios of BrO can result in low to moderate enhancements of the column, if the vertical extent of enhanced BrO is shallow (e.g., Sihler et al., 2012). On the other hand, numerous studies that have examined enhancements of satellite BrO are consistent with the time and place of elevated tropospheric BrO mixing ratios from suborbital observations only when the enhancement of BrO occurs either in a deep boundary layer or in the free troposphere (e.g., Choi et al., 2012; Peterson et al., 2017; Salawitch et al., 2010).

While model (Toyota et al., 2011; Yang et al., 2008, 2010) and observation/model studies of ozone-depleted air (Jones et al., 2009) suggest a connection between high BrO and blowing snow, very few in situ or ground-based measurements of BrO have been made in the presence of blowing snow (Hönninger et al., 2004; Hönninger & Platt, 2002). Blown snow particles and associated severe weather conditions pose a substantial challenge to most in situ and ground-based measurements techniques. However, there are field studies that support coincident BrO explosions and blowing snow events or blowing snow-generated sea-salt aerosols (SSAs). Jones et al. (2009) reported that enhanced BrO and depleted boundary layer ozone were coincident with high wind speeds and saline blowing snow in the Antarctic. In the Arctic, Frieß et al. (2011) showed elevated BrO coincident with wind speeds in excess of 5 m/s, which caused snow and ice particles to become airborne, during OASIS campaign conducted at Barrow, Alaska, in spring 2009. In addition, Jacobi et al. (2012) showed that bromide undergoes more complex behavior than other sea-salt components during a blowing snow event including transformation into volatile compounds.

Satellite observations of BrO can provide useful information to examine the relationship between BrO enhancements and blowing snow. For example, Yang et al. (2010) used GOME tropospheric column measurements to evaluate simulated bromine chemistry, and Theys et al. (2011) reported that the hypothesis of bromine release from blowing snow is supported by tropospheric column BrO data from GOME-2 for cases observed in 2007 and 2008. Finally, Nghiem et al. (2012) suggested that the high BrO events observed at Amundsen Gulf during the OASIS campaign may be associated with the rising air parcels that originate over both first-year and mixed sea ice, implying a connection between high tropospheric BrO and meteorology that is consistent with our findings shown below.

In this study, we investigate the connection between tropospheric BrO explosions and blowing snow events by utilizing daily images and the long-term record of OMI BrO observations. We infer occurrences and extents of BrO explosions using tropospheric column BrO estimates derived from OMI on board the NASA Aura satellite, as detailed in section 2.1, and simulate the SSAs generated from wind-driven blowing snow events with the Goddard Earth Observing System Version 5 (GEOS-5) model (section 2.2). Ground-based measurements of total and stratospheric columns of BrO (section 2.3) are used to evaluate OMI total and model-based stratospheric columns BrO used in this study in section 3.1. Cloud-Aerosol LIdar with Orthogonal Polarization (CALIOP) blowing snow detection measurements (section 2.4) are used to evaluate GEOS-5 simulated blowing snow SSA in section 3.2. Moderate Resolution Imaging Spectroradiometer (MODIS) daily pan-Arctic sea ice lead maps (section 2.5) and airborne active bromine measurements from the National Oceanic and Atmospheric Administration (NOAA) Aerosol, Radiation, and Cloud Processes affecting Arctic Climate (ARCPAC) campaign (section 2.6) are used to investigate an exemplary case in section 3.3.5. Weekly sea ice age maps from National Snow and Ice Data Center (NSIDC) are used to determine the first-year sea ice area (section 2.7). We conduct case studies of BrO explosions associated with blowing snow (section 3.3). We also examine the interannual variability and correlation of the frequencies of BrO explosions, blowing snow SSA emission, and first-year sea ice area (section 3.4).

2. Materials and Methods

2.1. OMI Tropospheric Column BrO

We derive tropospheric vertical column density (VCD) of BrO using the residual method with total BrO slant column densities (SCD) derived from OMI (OMBRO product; section 2.1.1), a climatology of model-estimated stratospheric column BrO (section 2.1.2), and air mass factors (AMF) calculated from the LInearized Discrete Ordinate Radiative Transfer model (Spurr et al., 2001). Each component is described below.

2.1.1. OMI Total BrO SCD

OMI is a nadir-viewing hyperspectral UV and visible radiometer (Levelt et al., 2006, 2017) that has been flying on the NASA Aura satellite since the middle of 2004. Aura is in a Sun-synchronous polar orbit with a local overpass time of ~13:30 at the equator. The full width at half maximum spectral resolution of the OMI UV-2 channel used to retrieve BrO columns is approximately 0.5 nm. The OMI swath width is ~2,600 km. The spatial resolution of the OMI UV-2 channel is approximately 13×24 km^2 at the swath center and significantly larger at the swath edges. The wide swath of OMI provides multiple daily observations at high latitudes in spring and daily global coverage at low and middle latitudes. An obstruction outside the instrument that produces radiance errors (known as the "row anomaly") reduced the swath coverage mainly after May 2008; we exclude the affected pixels in our analysis according to quality flags provided in the Level 1B OMI data set (Claas et al., 2010).

OMI BrO SCDs are retrieved by fitting a model function to OMI UV backscattered radiance, using a nonlinear least squares minimization approach (Suleiman et al., 2018). The model consists of the OMI-observed solar irradiance, attenuated by molecular absorption by BrO (the target gas), O_3, NO_2, HCHO, and SO_2, as well as inelastic rotational Raman scattering (also known as the Ring effect), plus closure polynomials. The spectral fitting window for the OMI algorithm is 319 to 347.5 nm. Absorption cross sections for BrO at 228 K from Wilmouth et al. (1999) are used. The uncertainty of OMI BrO total column related to spectral fitting ranges from about 15% to 51% (Kurosu & Chance, 2011).

2.1.2. Model-Estimated Stratospheric Column BrO

We estimate stratospheric column BrO using the dynamic climatology of Theys et al. (2009, 2011), which is based on the Belgian Assimilation System for Chemical ObsErvations model (Theys et al., 2009). Theys et al. (2009) provided stratospheric BrO column as a function of latitude and longitude throughout the globe, based on their model simulation performed for three years (April 2003 to March 2006). They assumed an inorganic bromine (Br_y) supply by very short lived bromocarbon to the stratosphere of 6 parts per trillion by volume (pptv) that includes 5 pptv of Br_y from dibromomethane (CH_2Br_2) source gas injection and 1 pptv of inorganic product gas injection of decomposed bromocarbons.

In order to build the dynamic climatology, the relationship between stratospheric O_3 and Br_y is utilized to prescribe Br_y abundances as a function of total ozone column. Solar zenith angle (SZA) is similarly used to parameterize photochemistry, such that the resulting BrO corresponds to the time of an OMI overpass. The stratospheric NO_2 column is used to account for the amount of Br_y that is present in the form of $BrONO_2$, a major reservoir species. The dynamic climatology consists of a set of Br_y profiles as a function of month, latitude, and the total ozone column and a set of profiles of Br_y to BrO partitioning ratio at the OMI overpass time as a function of month, latitude, SZA, and the stratospheric NO_2 column. We use the OMI-TOMS (OMTO3) total ozone product (McPeters et al., 2008) and stratospheric column NO_2 from the NASA Global Modeling Initiative model (Duncan et al., 2007; Strahan et al., 2007) as inputs for the dynamic climatology. We use tropopause pressure from Modern Era Retrospective analysis for Research and Applications (MERRA; Rienecker et al., 2011) to integrate the BrO profiles from the climatology to obtain the stratospheric BrO column.

We have based our analysis on the stratospheric BrO column climatology of Theys et al. (2009) because this method is computationally efficient, straightforward, and robust. This climatology has undergone extensive evaluation using multiple ground-based measurements spanning many years (Theys et al., 2009). A stratospheric BrO mixing ratio profile is found as a function of month, latitude, SZA, total column O_3, and stratospheric column NO_2. Also, this framework allows us to account for the negative trend in stratospheric bromine loading due to the slow, gradual decline in the abundance of substances regulated by the Montreal Protocol over the time period of the study. One drawback to the Theys et al. (2009) method is the use of total column O_3, which is assumed to act as an inert tracer. This approach becomes an inaccurate way to estimate stratospheric BrO during times when column O_3 is strongly affected by chemical loss, such as occurred during

spring 2011 (Manney et al., 2011). Therefore, data collected in March 2011 have been excluded from the time series analysis in section 3.4.

2.1.3. Tropospheric BrO VCD

Tropospheric column BrO is estimated from satellite total column BrO retrievals using the residual method. Here we provide a brief explanation of this method (see Choi et al., 2012; Theys et al., 2011, for details).

Tropospheric BrO vertical column densities (VCD_{Trop}) can be obtained from OMI BrO total slant column (SCD_{Total}, in section 2.1.1) by (1) subtracting the stratospheric BrO columns (VCD_{Strat}, in section 2.1.2) and (2) applying stratospheric and tropospheric AMF (AMF_{Strat} and AMF_{Trop}, respectively):

$$VCD_{Trop} = \frac{SCD_{Trop}}{AMF_{Trop}} = \frac{(SCD_{Total} - SCD_{Strat})}{AMF_{Trop}} = \frac{(SCD_{Total} - VCD_{Strat} \cdot AMF_{Strat})}{AMF_{Trop}}. \quad (6)$$

AMF_{Trop} is calculated at 344.6 nm using the LIDORT model (Spurr et al., 2001). For the calculation of AMF_{Trop}, we use a clear scene assumption as well as the composite BrO profile obtained from airborne measurements during the NASA Arctic Research of the Composition of the Troposphere from Aircraft and Satellites (ARCTAS) campaign as an a priori profile (Choi et al., 2012). The estimated AMF_{Strat} provided in the OMI total BrO column product is used in this calculation. We include negative values of tropospheric column BrO in pixels where $SCD_{Strat} \geq SCD_{Total}$. The fraction of negative pixels is less than 2%.

We filter data according to several criteria: (1) we use data only where the estimated surface reflectivity >0.6, because the UV satellite measurement is not very sensitive to lower tropospheric BrO when the surface is dark (Choi et al., 2012; Theys et al., 2011). In other words, we obtain tropospheric column BrO only where the surface is covered by snow or ice. (2) We attempt to remove data that are substantially affected by clouds, using the difference between the OMI rotational Raman cloud pressure and the terrain pressure. Data are retained only when this difference is <100 hPa (Vasilkov et al., 2008). Vasilkov et al. (2008) showed with radiative transfer calculations that clouds with optical thickness greater than about 15 (that they refer to as "shielding clouds") should be detected with these criteria. They showed good agreement of OMI-detected clouds over snow/ice with coincident CloudSat-detected optically thick clouds. The retained tropospheric column BrO data exhibit little to no correlation with the OMI O_2-O_2 cloud scene pressure deduced using the OMCLDO2 product, which supports the notion that scientific conclusions are not altered by the effect of light path enhancement by clouds (see Figures S1–S4 in the supporting information). (3) We only use data with SZA <84° for daily map analyses in section 3.3 and <80° elsewhere, because the uncertainties at SZAs larger than 84° are very high due to increased Rayleigh scattering, interference by O_3, and the BrO photochemistry varying along the light path. Data for which 80° ≤ SZA < 84° are included in daily maps, since these data may be used for qualitative interpretations, although they are not suitable for quantitative analysis. We note that tropospheric column BrO may be filtered out even where total and stratospheric columns are available, for example, due to optically thick clouds. In the maps of BrO columns in this study, we show data only where OMI tropospheric column BrO passed all of the filtering criteria.

2.2. GEOS-5 Simulations of Blowing Snow SSA

We use the GEOS-5 Data Assimilation System (GEOS-DAS) to estimate SSA emission generated from wind-driven blowing snow. The GEOS-DAS, developed by NASA Global Modeling and Assimilation Office, is composed of a global circulation model (GCM) and an analysis system (Rienecker et al., 2008) along with other components including a fully coupled aerosol transport module based on the Goddard Chemistry, Aerosol, Radiation, and Transport model (Chin et al., 2002). For this study, the GCM and aerosol module were run at a c48 horizontal resolution (corresponding to 2° × 2°) with 72 vertical layers between the surface and about 80 km. The model was run in a replay mode; we do not assimilate the OMI tropospheric BrO column measurements in the GEOS-5 model, and the simulated SSA does not interact with aerosol-related dynamics in the model. The replay mode uses previously computed analyses of the meteorological state every 6 hr (i.e., winds, temperature, and specific humidity) as initial states for the GCM (Buchard et al., 2015). The analyzed fields are obtained from the MERRA (Rienecker et al., 2011), a static version of the GEOS-5 DAS that is used for reanalysis spanning the satellite era. In the replay mode, the aerosols are directly transported but are not used for radiative transfer calculations within the GCM. The parameterized SSA emission used within this system is described below. We also use MERRA meteorological fields to investigate the relationship between Arctic tropospheric BrO (derived from OMI data) and climatological factors. The spatial resolution of the MERRA fields used in this investigation is 1/2° latitude × 2/3° longitude, finer than the fields used to run the simulation.

We derive the SSA emission flux from wind-driven blowing snow events over Arctic sea ice using a method similar to that of Yang et al. (2008). The SSA production is parameterized as a two-step process: (1) saline snow particles (i.e., wet sea-salt particles) are blown into the atmosphere when the wind speed exceeds the temperature-dependent threshold and (2) the lifted snow particles achieve complete drying by sublimation and become dry sea-salt particles. Henceforth, we refer to these particles as "blowing snow-generated SSAs."

The threshold wind speed at 10-m altitude for a blowing snow event to occur can be expressed as a function of ambient temperature (T_a, in Celsius):

$$U_t = 6.975 + 0.0033(T_a + 27.27)^2 \text{ [m/s]}. \tag{7}$$

With this formula, the minimum threshold wind speed is achieved at 245.88 K (or −27.27 °C). Snow tends to be wet and the embedded water leads to the greater cohesion of the snowpack at higher temperatures (~0 °C), while cohesion associated with strengthening elastic and frictional forces reduces the capacity of the wind to displace snow from the surface at lower temperatures (Déry & Yau, 1999).

The size distribution of the lifted snow particles is parameterized as a two-factor gamma function:

$$f(d_i) = \frac{e^{d_i/\beta} \cdot d_i^{\alpha-1}}{\beta^{\alpha} \cdot \Gamma(\alpha)}, \tag{8}$$

where d_i is snow particle diameter, α and β are, respectively, shape and scale parameters, and Γ is the gamma function (Schmidt, 1982). The mean diameter is given as $\bar{d}_i = \alpha \cdot \beta$. We take values of $\alpha = 2$ and $\bar{d}_i = 75$ μm from the model study of Yang et al. (2008) and measurements by Mann et al. (2000), giving β of 37.5 μm.

The lifted snow particles are assumed to achieve complete drying by sublimation. For a lifted snow particle, the diameter of the corresponding dry sea-salt particle is determined by the size and the salinity of the initial snow particle. We obtain the dry SSA particle size distribution using the snow salinity psu (practical salinity unit, normally measured in gram per kilogram saltwater) frequency distribution function provided by Massom et al. (2001) and used by Yang et al. (2008, 2010). The dry SSA emission flux (Q_{SSA}) can be expressed as follows:

$$Q_{SSA} = \frac{Q_s}{1000} \int_0^{\infty} \int_0^{\infty} f(\mathrm{d}_i)\zeta\psi(\zeta)\mathrm{d}(\mathrm{d}_i)\mathrm{d}\zeta, \tag{9}$$

where Q_s is blowing snow sublimation flux, ζ is the snow salinity, and $\psi(\zeta)$ is the snow salinity frequency distribution function (Yang et al., 2008). With this parameterization, the SSA emission flux is proportional to the blowing snow sublimation flux. We employ the parameterization of bulk snow model by Déry and Yau (1999), where the blowing snow sublimation flux is described as a function of wind speed, relative humidity, and snow age.

Salinity is an important factor related to microphysical processes of bromine release from snow, because SSA emission from blowing snow depends on snow salinity. Particularly in the parameterization used in equation (9), the probability density function (PDF) of snow salinity is necessary. Massom et al. (2001), conducted in Antarctica, is the only study to our knowledge that provides a published PDF for snow salinity. While a median value of Antarctic snow salinity given by Massom et al. (2001) is ~3.125 psu, the median snow salinity measured in the Arctic ranges from ~0.0005 psu (fresh snow, Toom-Sauntry & Barrie, 2002) to ~3.84 psu (snow on thin first-year sea ice surface, Krnavek et al., 2012). Moreover, Krnavek et al. (2012) reported that snow over thin and thick first-year sea ice is more saline (medians ~3.84 and ~1.47 psu, respectively) than over multiple-year sea ice (median ~0.015 psu). If this was the case over the entire Arctic, we would expect less blowing snow SSA mass emission flux with smaller particle sizes from multiple-year sea ice than presented in this study, as less salinity results in smaller particle size in parameterization by Yang et al. (2008).

We performed an additional calculation to assess the role of first-year sea ice in driving the BrO explosions, as viewed from space. For this sensitivity study, we assumed that the snow salinity PDF of Massom et al. (2001) occurred only over first-year sea ice and that the salinity, and hence SSA emission, is 0 over the multiple-year sea ice. Results are presented in sections 3.2 and 3.4 comparing the two assumptions regarding SSA emission: (1) SSA emission over sea ice of any age and (2) SSA emission over first-year sea ice only. For most of the results shown in section 3.3, we use the assumption of SSA emission over sea ice of any age because the results based on this assumption give overall better agreement with OMI tropospheric column BrO than the simulation that assumes modeled SSA emission only over first-year sea ice. Our sensitivity study is motivated

by Krnavek et al. (2012) and Toyota et al. (2011). Krnavek et al. (2012) reported that snow on first-year sea ice has higher salinity than that on multiple-year sea ice. Toyota et al. (2011) reported that their simulated BrO shows a better agreement with satellite measurements when assuming first-year sea ice is more effective in releasing active bromine than multiple-year sea ice.

We exclude dry SSA particles with diameters >10 μm due to their short lifetime in the atmosphere. Open oceans and surfaces without snow cover are neglected in the analysis since no blowing snow is expected from such surfaces. We also neglect inland Greenland, since the snowpack in this region is likely not saline enough to emit SSAs. We define "snow age" as the time elapsed since the last snowfall inferred from GEOS-5 snow precipitation flux and use a snow age factor (equation (5) of Yang et al., 2008) to address decreasing emission flux of blowing snow SSA over time. We assume that no blowing snow-generated SSA is produced for snow age >7 days, since the snow age factor to which Q_s in equation (9) is proportional behaves in a physically nonrealistic manner if snow age is greater than 7 days.

The GEOS-5 fields (such as SSA) are available every 3 hr. We sample the model fields at the time closest to the approximate OMI local overpass over the Arctic (14:00). The maximum time difference between the model and OMI overpass is 1.5 hr. The one exception is that, for 16–18 April 2008, the model output was sampled at a fixed time of 1:30 UTC near the North Pole because of the very patchy structure introduced by small differences in satellite overpass time near the pole.

2.3. Ground-Based BrO Column Measurements at Harestua

Ground-based BrO columns at Harestua, Norway (60°N, 11°E), are derived from vertical profiles retrieved by applying an optimal estimation method-based profiling algorithm to zenith-sky DOAS BrO SCD measurements at sunset (Hendrick et al., 2007). Zenith radiance spectra are analyzed in the 336 to 359-/345 to 359-nm wavelength range using a fixed reference spectrum corresponding to clear-sky noon summer conditions and the Wilmouth et al. (1999) absorption cross sections for BrO. Regarding the other DOAS settings, the main changes with respect to Hendrick et al. (2007) are the following: O_3 cross sections at 218 and 243 K from Brion et al. (1998), Daumont et al. (1992), Malicet et al. (1995), a Taylor expansion of O_3 SCD in wavelength and vertical optical depth as in Puķīte et al. (2010), and O_2-O_2 cross sections from Greenblatt et al. (1990).

To best ensure the photochemical matching between satellite and ground-based observations, only ground-based vertical profiles at the closest twilight period (sunset) have been photochemically converted to the OMI equator overpass time (~13:30 LT) by means of the stacked box photochemical model included in the profiling algorithm (see Hendrick et al., 2009, 2007, for more details). Twilight conditions (sunrise or sunset) are needed for the retrieval because it is the period of the day where the BrO SCD shows the strongest variation with SZA. The sensitivity of the zenith-sky observations to tropospheric BrO is increased by using for the DOAS analysis a fixed reference spectrum corresponding to clear-sky noon summer and low BrO absorption conditions.

2.4. CALIOP Blowing Snow Detection

The CALIOP lidar instrument was launched in April 2006, aboard the Cloud-Aerosol Lidar and Infrared Pathfinder Satellite Observation satellite, a joint mission between the French Centre National d'Études Spatiales and NASA (Winker et al., 2007, 2009). The CALIOP instrument has been used to detect the presence of blowing snow (Palm et al., 2011). The blowing snow product from CALIOP is binary: that is, either the presence or absence of blowing snow is reported. The diameter of CALIOP footprint is approximately 90 m. The spatial coverage of CALIOP measurements is up to latitude 82°N.

2.5. MODIS Daily Pan-Arctic Sea Ice Lead Maps

We use daily pan-Arctic sea ice lead maps by Willmes and Heinemann (2015) to investigate a BrO explosion event observed by OMI in terms of sea ice leads. A lead is defined by the World Meteorological Organization as a more than 50-m-wide crack in the ice, from several kilometers to hundreds of kilometers in length. Willmes and Heinemann (2015) use thermal-infrared data from the MODIS sensor aboard NASA's Terra and Aqua spacecraft to obtain Arctic sea ice lead maps. Over sea ice, their algorithm gives the following four categories: sea ice, lead, clouds (i.e., no data), and "artifact." By employing a conservative artifact class that contains 50% of true leads, sea ice leads are identified with high confidence (95%; see Willmes & Heinemann, 2015, for more details).

2.6. ARCPAC Airborne In Situ Active Bromine Measurements

We use airborne in situ chemical ionization mass spectroscopy "active bromine" (Br_2 + HOBr) measurements aboard the WP-3D aircraft during NOAA ARCPAC campaign in April 2008 (see Neuman et al., 2010, for details). In section 3.3.5, we investigate a BrO explosion event observed by OMI on 19 April 2008 that was coincident with high active bromine reported by the CIMS instrument on the WP-3D on this day during ARCPAC.

2.7. First-Year Sea Ice Area

We use maps of sea ice age provided by NSIDC (Tschudi et al., 2017). These estimates are based on remotely sensed sea ice motion and sea ice extent for the Arctic Ocean. These data are used for our case studies (maps) as well as our time series analysis (area of first-year sea ice).

3. Results

3.1. Evaluation of OMI and Model-Based BrO Columns

Figure 1 quantifies the consistency between the OMI total column BrO operational product and stratospheric column BrO from the model-based climatology by comparing these two time series with ground-based measurements from Harestua, Norway (60.2°E, 10.7°E), during March and April of years 2005 to 2011. Estimated uncertainties of the presented BrO columns are as follows: 14% for OMI total column BrO, 16% for ground-based total column BrO, 30% for model stratospheric column BrO, and 20% for ground-based stratospheric column BrO.

Figure 1a shows the time series of total columns BrO from OMI (black) and the ground-based measurement (red), and Figure 1b shows a scatter plot of the two total column BrO data sets. The OMI time series were obtained by averaging all data within a 2.5° latitude by 5.0° longitude box, centered over Harestua, on a daily basis. The uncertainties are also shown by the green error bars on Figure 1b. These comparisons can only be made for years 2005 to 2011, because retrievals from Harestua for later years are still being processed.

This analysis shows that OMI total column BrO is, on average, 13% higher than retrieved by the ground-based instrument. This overestimation could be caused by the difference in the fitting windows used by OMI (319–347.5 nm) and the ground-based retrieval (336–359 nm). It is well known that changing DOAS fitting windows can result in a difference of retrieved BrO column comparable to the offset shown in Figure 1a. Another possible explanation for the observed difference in the total column magnitudes is uncertainties in the AMFs used in both OMI and the ground-based retrievals. In terms of temporal variations, the OMI and ground-based total columns BrO exhibit a moderately positive correlation. Visual inspection shows similar temporal variations of the two time series, and most importantly, the agreement does not degrade over time. This result indicates that the instrumental degradation OMI (Schenkeveld et al., 2017) has a minimal effect on our analyses.

The scatter plot shown in Figure 1b illustrates that the two observations of total column BrO lie close to the one to one line. Figure 1b also includes the numerical value of reduced chi squared (χ^2_ν), the goodness of fit parameter. The value of χ^2_ν of 0.454 shows that the offsets of these two measurements of total column BrO are within the respective uncertainties. The data exhibit a correlation coefficient of 0.54, which is caused in part by the clustering of both data sets near the same mean value. The variability of total column BrO over Harestua is smaller than observed in other parts of the Arctic (i.e., Figure 2), because this inland site does not experience significant enhancements of tropospheric BrO.

Figure 1c shows time series of stratospheric column BrO (VCD_{Strat}), inferred as described in section 2.1.2, for the location of Harestua (black) as well as ground-based measurements of VCD_{Strat} at this site (red). We also present OMI total column O_3 (blue) in Figure 1c, because this quantity is used as part of the method to determine VCD_{Strat} (Theys et al., 2009). Figure 1d shows a scatter plot of the two data sets for VCD_{Strat}. The measured and modeled values of VCD_{Strat} agree to within 5%, lie close to the one to one line, and exhibit a value of reduced chi squared equal (χ^2_ν) to 0.135, which indicates excellent agreement to within the respective uncertainties.

The correlation coefficient for the two VCD_{Strat} data sets is 0.49, slightly lower than found for total column BrO. The largest difference between the two values of VCD_{Strat} occurs when total column ozone drops below ~280 DU (i.e., March 2011). Under this condition, the method for estimating VCD_{Strat} has a higher error. Henceforth, we exclude data acquired during March 2011 because chemical loss of stratospheric ozone in the Arctic for this winter led to extensive regions where column O_3 fell below 280 DU (Manney et al., 2011).

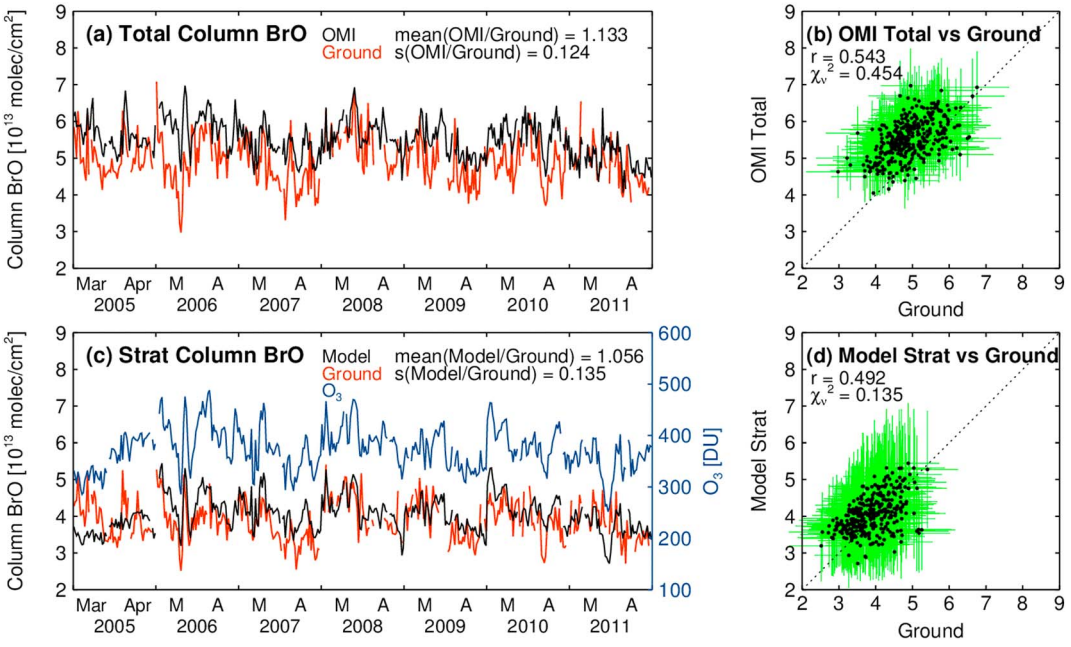

Figure 1. Time series and scatter plots comparing data used to derive OMI tropospheric column BrO and ground-based measurements during March and April for 2005–2011; (a) OMI operational total column BrO vertical column density (black) and ground-based total column BrO (red), (b) scatter plot between OMI operational and ground-based total columns BrO, (c) model-estimated stratospheric column BrO (black), ground-based stratospheric column BrO (red), and OMI total column O_3 (blue), and (d) scatter plot between model-estimated and ground-based stratospheric columns BrO. Estimated uncertainties of BrO columns are as follows: 14% for OMI total column BrO, 16% for ground-based total column BrO, 30% for model stratospheric column BrO, and 20% for ground-based stratospheric column BrO. OMI = Ozone Monitoring Instrument.

Evaluation and validation of tropospheric residual BrO is challenged by the fact that few observations of tropospheric column BrO exist in regions of the BrO explosions. We show in section 3.3.5 that limited in situ observations of BrO are well aligned with the crescent-shaped structure of enhanced tropospheric column BrO inferred from our analysis of the OMI data. Also, prior studies have shown fairly good agreement between tropospheric column BrO found from aircraft profiles and residual tropospheric column BrO found by a method similar to that used here (Choi et al., 2012; Liao, Huey, Scheuer, et al., 2012; Salawitch et al., 2010).

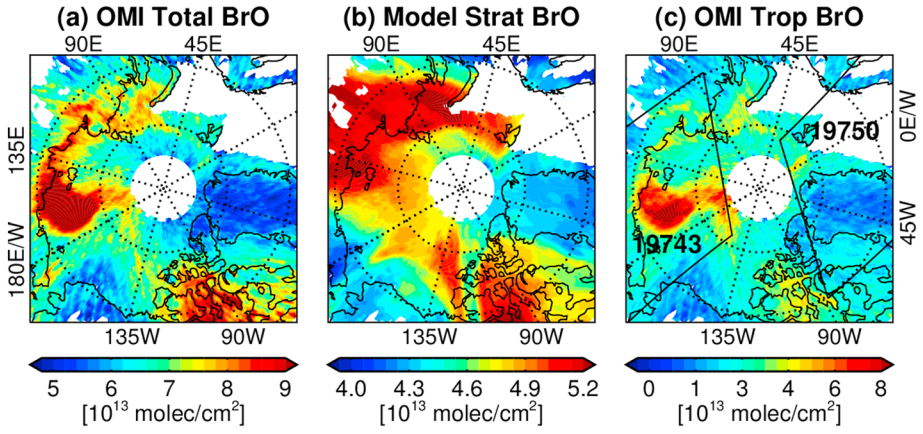

Figure 2. (a) OMI-observed total BrO column, (b) model simulated stratospheric BrO column, and (c) the derived OMI tropospheric BrO column, in which the locations of OMI orbits 19743 and 19750 are shown, for 1 April 2008. Regions for which OMI tropospheric column did not pass the filtering criteria (see the last paragraph of section 2.1.3) are denoted as white. OMI = Ozone Monitoring Instrument.

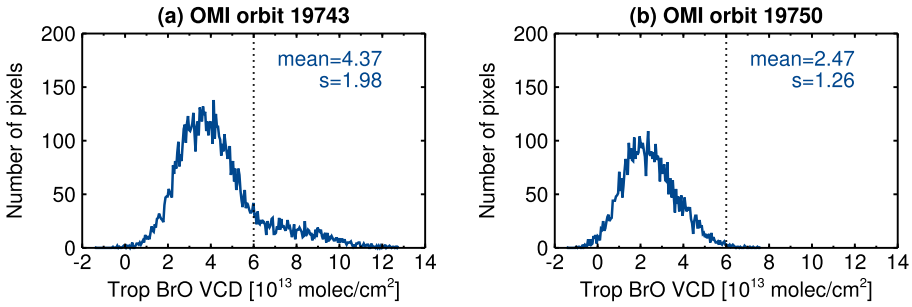

Figure 3. (a) Probability density functions of tropospheric column BrO observed from OMI orbit 19743. (b) Similar to (a) but for OMI orbit 19750. See Figure 2c for the location of each orbit. The threshold used to determine the BrO explosion is given by the vertical dotted line on each panel. OMI = Ozone Monitoring Instrument; VCD = vertical column density.

Figure 2 shows sample maps of OMI total column BrO (Figure 2a), the model stratospheric column BrO (Figure 2b), and the tropospheric column BrO (Figure 2c) derived using the residual method for 1 April 2008. This day includes a good example of a region with a tropospheric BrO explosion. The OMI total column BrO shows pronounced enhancements over the East Siberian Sea, the Canadian Archipelago, and Nunavut territory. Moderately high total column BrO is also present along the north coast of Russia and the Kara Sea. In contrast, OMI measured low total column BrO over inland Alaska and Greenland. The stratospheric column BrO is also elevated over the north coast of Russia and a narrow region along 120°W longitude, in addition to the Canadian Archipelago. Meanwhile, diminished stratospheric column BrO is observed over inland Greenland and Alaska, which agrees with the observed OMI total column BrO. The calculated OMI tropospheric column BrO reveals apparent enhancement over the East Siberian Sea, after all stratospheric structures have been removed from the OMI total column.

Figure 3 shows the PDFs of tropospheric column BrO for OMI orbit 19743 (left panel) and 19750 (right panel) on 1 April 2008 for observations obtained north of 65°N. The outlines of these orbits are shown in Figure 2c. The PDF for orbit 19743 includes an apparent BrO explosion. The PDF of tropospheric BrO column from orbit 19750 exhibits an almost normal distribution, with a mean and standard deviation of $\sim 2.5 \times 10^{13}$ and $\sim 1.3 \times 10^{13}$ molecules/cm^2, respectively. A noticeable feature for OMI orbit 19743 is a "tail" on the right side of the PDF, which indicates enhanced tropospheric column BrO. In contrast, the corresponding PDF from orbit 19750 (right panel of Figure 3) does not have a high-end tail.

We empirically choose a threshold tropospheric column of 6×10^{13} molecules/cm^2 to delineate BrO explosions; that is, BrO explosions are said to occur when VCD_{Trop} from OMI exceeds this threshold. The threshold is shown by the vertical lines in Figure 3. Data classified as being part of a BrO explosion represent approximately the top 5th percentile of tropospheric column BrO for the spring season (March and April). We note that when autocatalytic processes release labile bromine, this may involve numerous reactive bromine species. If activated bromine other than BrO (e.g., Br_2, Br, BrCl, BrI, and HOBr) is abundant, we can only observe this phenomenon if the bromine is transformed to BrO. In other words, high BrO indicates the presence of activated bromine species, but the reverse may not be always true.

As noted above, we use the term "BrO explosion" to refer to enhanced tropospheric column BrO ($>6 \times 10^{13}$ molecules/cm^2) observed over a large spatial scale by OMI. This term differs from the more general "bromine explosion" that commonly is used to denote the production of active bromine by autocatalytic chemical pathways that occur in the presence of sunlight (Wennberg, 1999).

Our correlation analysis demonstrates that the stratospheric influence on the total column BrO (i.e., the moderate correlation with total column O_3, as discussed in section 2.1.2) has been removed in our OMI-derived tropospheric column BrO used in section 3.3. While the maximum correlation coefficient between total column BrO and total column O_3 is 0.65 ($r^2 = 0.42$), that between tropospheric column BrO and total column O_3 is only 0.31 ($r^2 = 0.096$; see Figures S5–S8 in the supporting information).

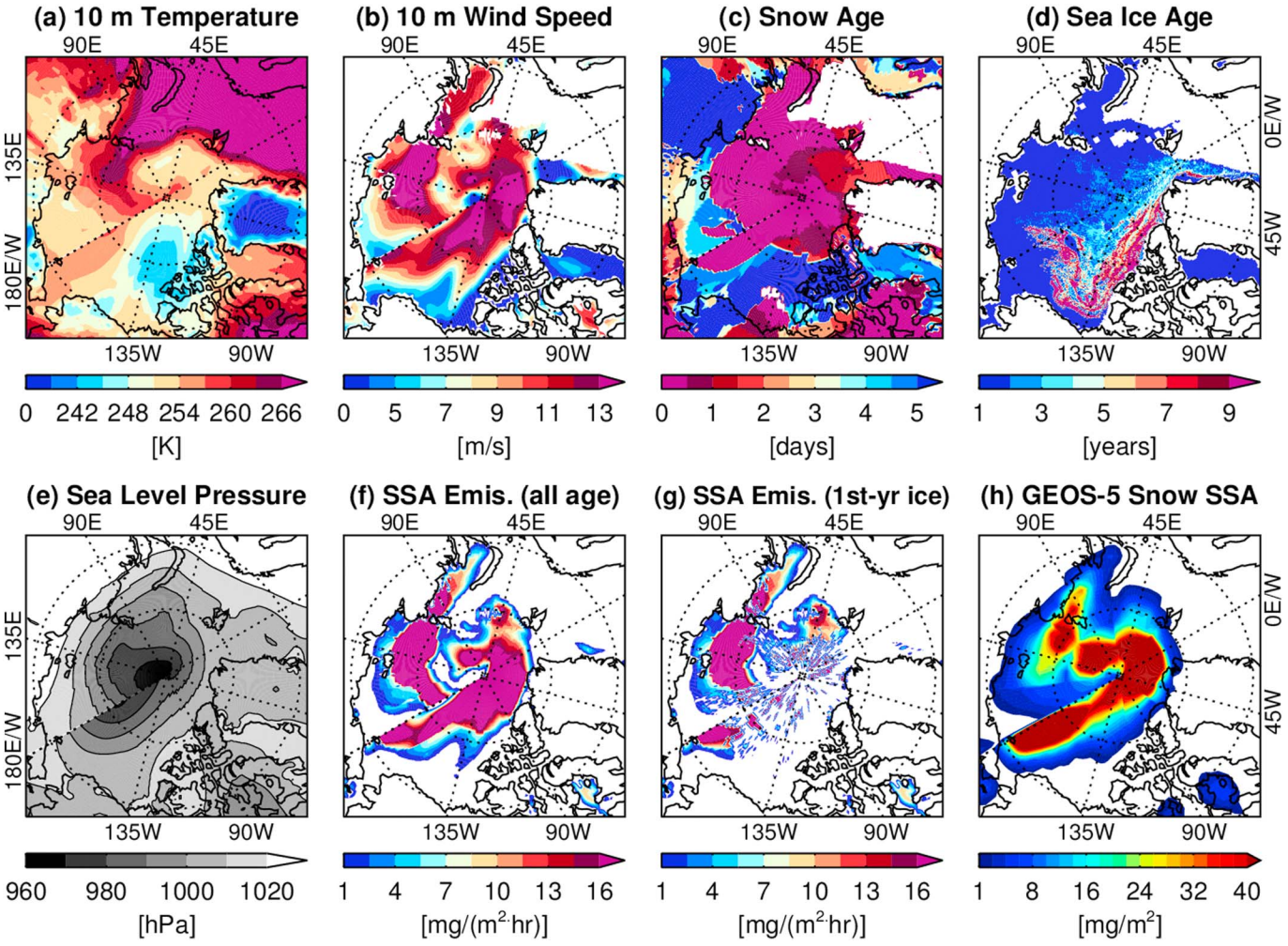

Figure 4. Meteorological data relevant to wind-driven blowing snow on 25 March 2007; (a) 10-m ambient temperature, (b) 10-m wind speed (not shown for areas without snow/ice cover), (c) snow age, (d) NSIDC sea ice age, (e) sea level pressure, (f) blowing snow-generated SSA flux assuming emission over sea ice of any age, (g) blowing snow SSA flux assuming emission only over first-year sea ice, and (h) GEOS-5 simulated blowing snow-generated SSA column mass, assuming emission over sea ice of any age. NSIDC = National Snow and Ice Data Center; SSA = sea-salt aerosol; GEOS = Goddard Earth Observing System.

3.2. Blowing Snow SSA Emission Flux

Figure 4 shows an example of relevant MERRA meteorological fields and the corresponding blowing snow-generated SSA emission flux on 26 March 2007, since this day contains a good example of blowing snow events. We also present BrO column data and column-integrated mass of GEOS-5 simulated blowing snow SSA for this day.

The ambient temperature (Figure 4a) determines the threshold speed over which the emission of blowing snow occurs. The 10-m ambient temperature was below 270 K over most parts of the Arctic circle, except for the Barents and Greenland Seas, on 25 March 2007. Unlike other parts of the Arctic Ocean, the Barents and Greenland Seas are covered by open ocean rather than sea ice. Ambient temperature over this area is >270 K (shown in purple) owing to the heat flux from the open ocean surface. The corresponding threshold wind speed over the Arctic ocean (covered by sea ice) and coastal regions ranges from 6 to 8 m/s (not shown). Figure 4b shows the 10-m wind speed from MERRA. We do not show the wind speed over the neglected area in inland Greenland (previously mentioned in the last paragraph of section 2.2), since we do not expect sea-salt-contaminated blowing snow events from such surfaces. Figure 4c shows the snow age over the area of interest, calculated from MERRA meteorological fields. Figure 4d shows an NSIDC sea ice age map. A large area of multiple-year sea ice appears from the north coast of Greenland to the Beaufort Sea, as well as over the Chukchi Sea. Sea level pressure is presented in a gray color scale, to provide the meteorologic

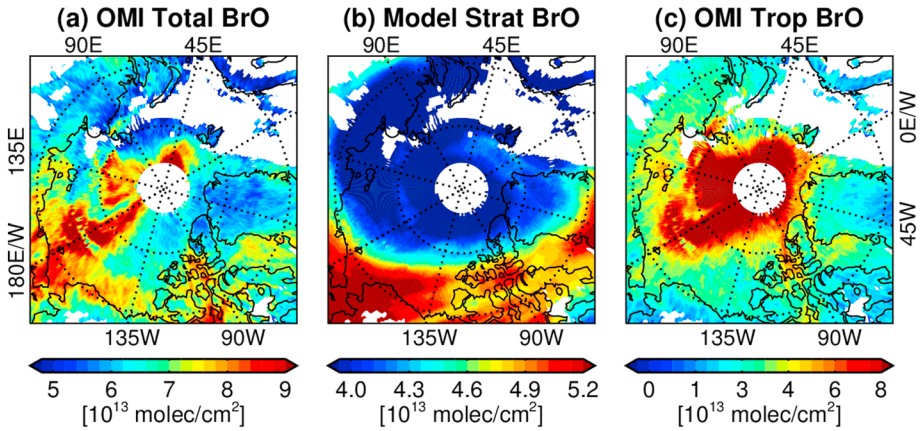

Figure 5. Similar to Figure 2 but for (a) OMI-observed total BrO column, (b) model simulated stratospheric BrO column, and (c) the derived OMI tropospheric BrO column, on 25 March 2007. Regions for which OMI tropospheric column did not pass the filtering criteria (see the last paragraph of section 2.1.3) are denoted as white. OMI = Ozone Monitoring Instrument.

context of the blowing snow events (Figure 4e). A low-pressure system near the North Pole results in a large pressure gradient.

Figure 4f shows the derived blowing snow SSA emission flux generated from wind-driven blowing snow events, assuming SSA emission over sea ice of any age. The occurrence of blowing snow coincides with regions of the high pressure gradients (Figure 4e) and thus strong winds (Figure 4a) owing to the low-pressure system. In this parameterization, many blowing snow events are associated with polar cyclones. Column-integrated mass of the simulated GEOS-5 blowing snow SSA based on this emission is shown in Figure 4h, which exhibits the spatial patterns similar to the emission flux (Figure 4f).

In Figure 4g, we also present a map of blowing snow SSA emission flux assuming that blowing snow SSA emission occurs only over first-year sea ice, to test the assumption that the BrO explosion is driven by first-year sea ice. According to Krnavek et al. (2012), the surface snow on the first-year sea ice is highly saline, while the surface snow on the multiple-year sea ice is not. With this assumption, no SSA is emitted near the North Pole (0–180°W longitude, over 80°N latitude) since this area is covered by multiple-year sea ice (see Figure 4d).

Figure 5 presents maps of OMI total column BrO (Figure 5a), the model stratospheric column (Figure 5b), and the derived tropospheric column BrO (Figure 5c) on 25 March 2007, the same date as Figure 4 to allow readers to compare all relevant quantities. Total column BrO shows enhancement over the Bering Strait, Chukchi Sea, north coast of Alaska, and Canadian Archipelago. A large zonal structure of enhanced stratospheric column BrO appears, stretching from the Bering Strait, crossing the Canadian Archipelago, to southern Greenland. After subtraction of the stratospheric column and AMF correction, the resulting tropospheric column BrO exhibits different spatial patterns than total column BrO. The tropospheric column shows enhancement near the North Pole and a part of this structure stretches along 180°E/180°W longitude.

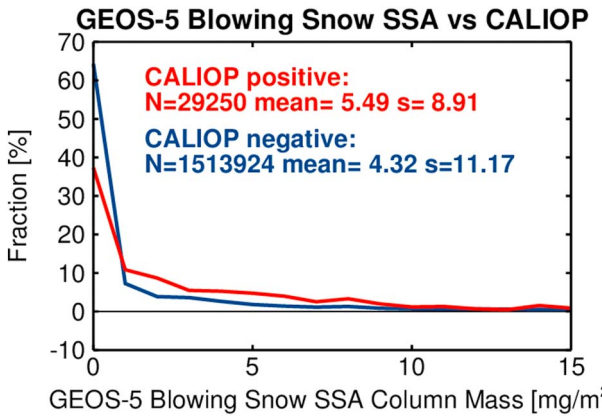

Figure 6. Histograms of GEOS-5 blowing snow SSA column mass coincident with CALIOP measurements collected during the two case studies in March 2007 and 2008; Red: CALIOP positive, that is, reports blowing snow events; Blue: CALIOP negative, that is, does not report blowing snow events. GEOS = Goddard Earth Observing System; SSA = sea-salt aerosol; CALIOP = Cloud-Aerosol LIdar with Orthogonal Polarization.

We note that the spatial structure of enhanced tropospheric column BrO (Figure 5c) resembles that of SSA column mass assuming emission over sea ice of any age (Figure 4h). A simulation based on emission over first-year sea ice only would cause disagreement between the SSA and OMI tropospheric BrO in this particular case, due to the lack of emission over multiple-year sea ice near the North Pole (Figure 4g).

Next, a comparison between CALIOP blowing snow detections and GEOS-5 simulated SSA column mass is summarized. Figure 6 shows histograms of the GEOS-5 SSA column mass for locations where CALIOP reports the presence of blowing snow (positive, red) as well as column

mass for regions where CALIOP does not report blowing snow (negative, blue). These histograms are based on the sampling of our model output for the two case studies in sections 3.3.1 and 3.3.2 (i.e., 24–28 March 2007 and 11–15 March 2008). We sample GEOS-5 grid boxes only at the time and the place of CALIOP measurements of blowing snow. This figure shows that the highest values of SSA column mass tend to be associated with positive detections by CALIOP (i.e., the red curve lies above the blue curve, for SSA column mass >1 mg/m^2). On the other hand, for the lowest value of blowing snow SSA column mass found in the model (mass <1 mg/m^2), CALIOP more often reports negative (no blowing snow) than positive (presence of blowing snow; i.e., the blue curve lies above the red curve). However, the difference of the two distributions shown in Figure 6 is not statistically significant at the one sigma level.

The CALIOP blowing snow data are an experimental product with large uncertainty (Palm et al., 2011). Also, CALIOP "blowing snow detection" and GEOS-5 "blowing snow-generated SSA emission flux" represent different aspects of blowing snow (i.e., presence of blowing snow versus flux of saline aerosols). Despite the difference in the size of the CALIOP footprint (~90 m) compared to the spatial resolution of GEOS-5 (2° × 2°), limited spatial coverage of CALIOP up to 82°N, as well as the other measurement uncertainties and possible model errors, the GEOS-5 blowing snow SSA product does give overall higher column mass where CALIOP reports positive blowing snow detection.

3.3. Case Studies

Choi et al. (2012) investigated links between apparent BrO explosions and meteorological fields. They reported that the examined BrO explosion events were associated with high pressure gradients, high near-surface wind speeds, and high PBL heights.

In this study, we build upon this prior work by simulating the SSAs emitted from wind-driven blowing snow events. We examine, in detail, two BrO explosion events that occurred in conjunction with blowing snow events. These BrO explosion events have been previously studied using GOME-2 satellite data (Begoin et al., 2010; Nghiem et al., 2012) as well as shipborne LP-DOAS measurements (Pöhler et al., 2010) but not in the context of blowing snow-generated SSAs. The sea ice age map for the case in section 3.3.1 is provided in Figure 4d, and the sea ice maps for other case studies (sections 3.3.2–3.3.4) are presented in Figure S11 in the supporting information.

3.3.1. The 24–28 March 2007 Event

Figure 7 details a large BrO explosion associated with a strong polar cyclone in late March 2007. Begoin et al. (2010) investigated this event in the context of long-range transport of tropospheric BrO, possibly involved with recycling of BrO due to gas and aerosol phase chemistry. We extend their analysis with a focus on the connection between blowing snow and tropospheric BrO explosions. Figure 7 shows maps of the column-integrated mass of blowing snow-generated SSAs at 19:30 UTC (top) and daily gridded OMI-derived tropospheric column BrO (bottom) for five days of interest (each column represents a day).

First, we show the onset of the BrO explosion during 24–25 March 2007. Areas with high amounts of blowing snow-generated SSAs coincide with a low-pressure system near the North Pole on 24 March 2007. Even with this well-developed structure of the SSAs, we see high BrO tropospheric column amounts only in a small area at north of Greenland. On 25 March 2007, a large area of enhanced tropospheric BrO column associated with high SSA is observed by OMI.

During 26–28 March 2007 (third to fifth columns of Figure 7), the spatial structure of the SSAs moved eastward and dissipated as the low-pressure system diminished. OMI tropospheric column BrO maps show that the enhanced BrO structure similarly moved eastward. In this period, the coincident MERRA PBL height (not shown) ranges from 1 to 1.5 km, which may allow BrO injection into the Arctic free troposphere; such cases have been observed during the ARCTAS field campaign (Choi et al., 2012; Salawitch et al., 2010). This result agrees with the previous study of Begoin et al. (2010), who reported possible transport of BrO to altitudes up to 3 km. The presence of the blowing snow during this event was confirmed by CALIOP (see Figure S9 in the supporting information).

Figure 8 presents box and whisker plots for GEOS-5 column mass of blowing snow SSA, wind speed at 10 m, and temperature at 10 m, all versus OMI tropospheric column BrO. Correlation coefficients between each variable and collocated OMI BrO column are also provided. The box and whisker plots and correlation coefficients are obtained over the entire Arctic area poleward of 65°N. Data points with negative BrO column are included in the calculation of correlation coefficients. We show BrO bins where the number of data points is greater

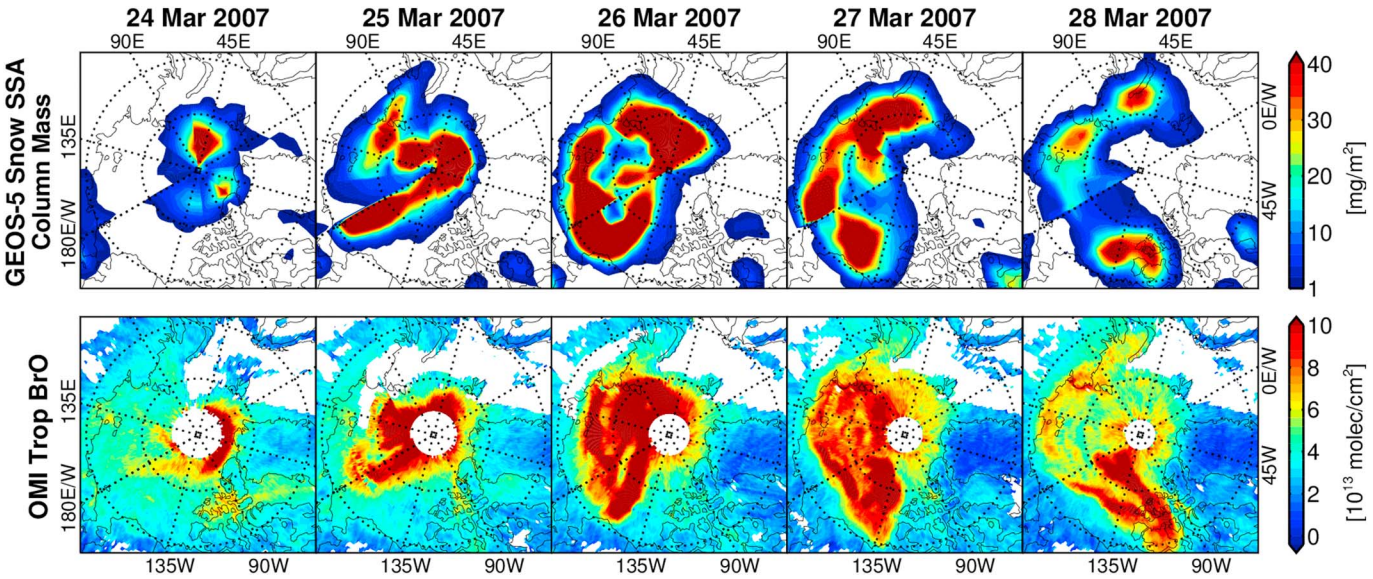

Figure 7. (top) Column-integrated mass of blowing snow-generated SSAs simulated using GEOS-5, and (bottom) OMI-observed tropospheric column BrO for 24–28 March 2007. For top panels, regions where OMI tropospheric column did not pass the filtering criteria (see the last paragraph of section 2.1.3) are denoted as white. For bottom panels, regions where SSA column mass <1 mg/m^2 are denoted as white. GEOS = Goddard Earth Observing System; SSA = sea-salt aerosol; OMI = Ozone Monitoring Instrument.

than 1% of the total number of data points in the box and whisker plots. The plots show 10th, 25th, median, 75th, and 90th percentile distributions of these variables as a function of OMI tropospheric column BrO for each 1×10^{13}-molecules/cm^2 step of the BrO column. The moderately positive correlation ($r = 0.60$) between the SSA column mass and OMI BrO column gives quantitative support for the connection between these two quantities (Figure 8a). On the other hand, wind speed at 10 m (Figure 8b) and temperature at 10 m (Figure 8c) do not exhibit significant correlations with OMI tropospheric column BrO ($r = 0.24$ and -0.14, respectively).

3.3.2. The 11–15 March 2008 Event

Here we examine an event that occurred near the Canadian Archipelago, Amundsen Gulf, and the northern coast of Canada in March 2008. Pöhler et al. (2010) reported enhanced tropospheric BrO in this region using shipborne LP-DOAS measurements, and Nghiem et al. (2012) investigated this case in the context of first-year (seasonal) sea ice using GOME-2 total column BrO. We extend these analyses by including estimates of blowing snow emission.

Figure 9 shows maps of blowing snow-generated SSAs and tropospheric column BrO for 5 days in March 2008. On 11 March 2008, a region of high SSAs occurred in the vicinity of the north of Beaufort Sea (80°N, 135°W) and a trace of enhanced tropospheric BrO coincides with the southern part of the high SSA structure.

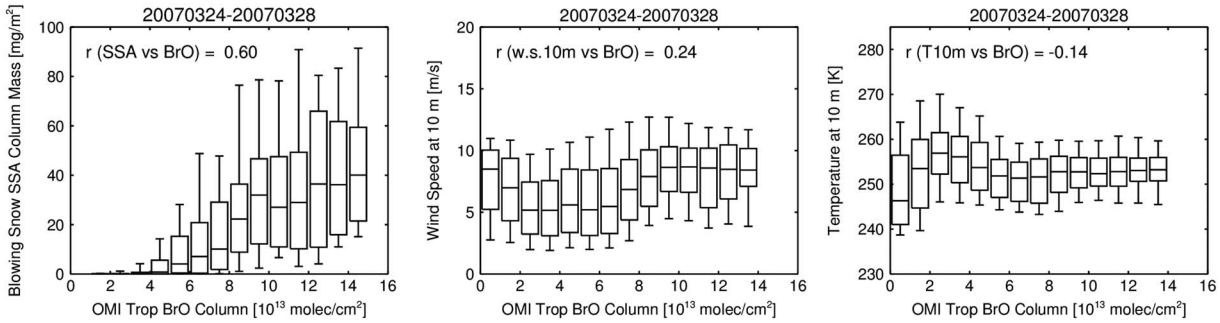

Figure 8. Box and whisker plots showing 10th, 25th, median, 75th, and 90th percentiles for (a) Goddard Earth Observing System-5 simulated blowing snow-generated SSA, (b) wind speed at 10 m, and (c) temperature at 10 m, each as a function of OMI-observed tropospheric column BrO, for each 1×10^{13} molecule/cm^2 step of BrO column during 24–29 March 2007. All data poleward of 65°N are used to obtain the correlation coefficients, while box and whisker plots show bins only where the numbers of data points are greater than 1% of the total number of data points. OMI = Ozone Monitoring Instrument; SSA = sea-salt aerosol.

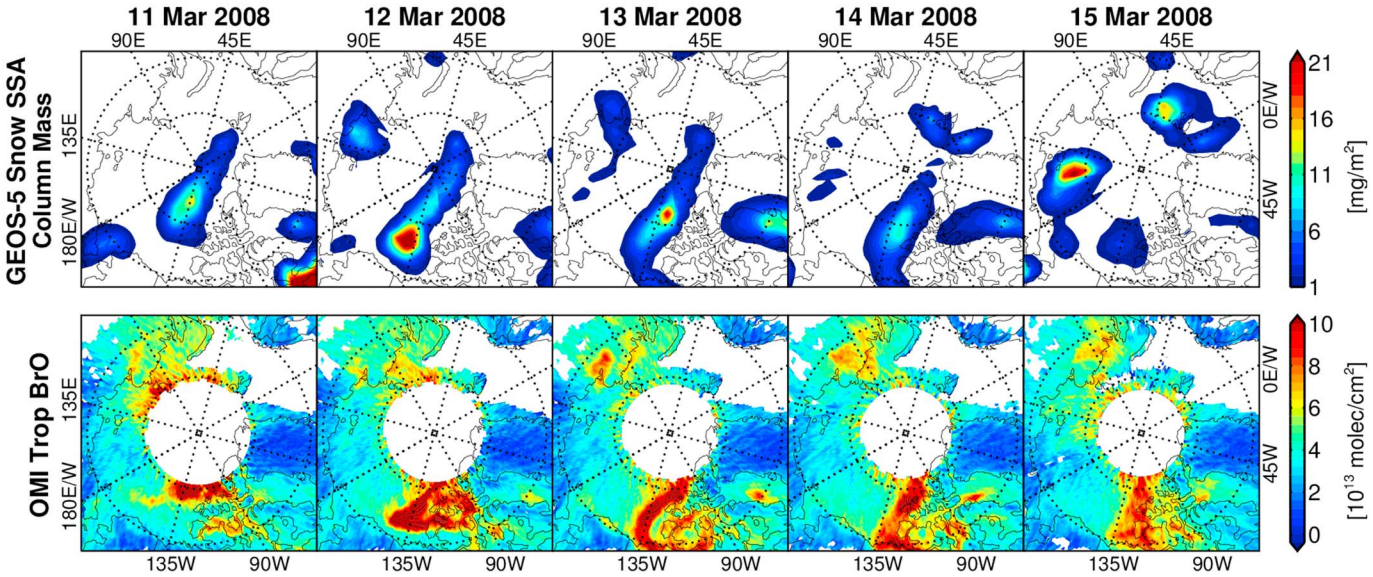

Figure 9. Similar to Figure 7 but for (top) column-integrated mass of blowing snow-generated SSAs simulated using GEOS-5, (bottom) OMI-observed tropospheric column BrO for 11–15 March 2008. For top panels, regions for which OMI tropospheric column did not pass the filtering criteria (see the last paragraph of section 2.1.3) are denoted as white. For bottom panels, regions where SSA column mass < 1 mg/m^2 are denoted using white. SSA = sea-salt aerosol; OMI = Ozone Monitoring Instrument; GEOS = Goddard Earth Observing System.

On 12 March 2008, the structure of high SSAs moved south, where the tropospheric column BrO showed an increasing enhancement in a V-shaped area in the Beaufort Sea. On 13 March 2008, the structure of high SSAs stretches to the north coast of Canada toward where enhanced BrO column was observed. The map of GEOS-5 SSA emission flux (see color contours of Figure S10 in the supporting information) indicates that this BrO feature could be transport of emitted SSAs rather than in situ emission. The structure of high SSA diminishes after 15 March 2008, and the signature of the BrO explosion begins to fade as well (not shown). A region of high SSA but no enhancement of tropospheric BrO appears at the north coast of Russia on 15 March 2008. We note that the ice surface at this region is mostly first-year sea ice (see Figure S11a), which we would expect to be associated with enhanced BrO. However, high SSA without enhanced BrO may be explained by the presence of bromide-depleted SSA. On the other hand, it is possible that the simulation of high SSA for this region is due to a modeling error.

Nghiem et al. (2012) reported a blowing snow event at Amundsen Gulf on 16 March 2008 and suggested the possible connection of this event to the diminishment of high BrO. We note that this is a hypothesis based on observations of blowing snow from a single location at Amundsen Gulf (i.e., the location of icebreaker Canadian Coast Guard Ship *Amundsen*). We now reexamine this event in the regional context provided by OMI, CALIOP, and MERRA data. The MERRA meteorological data suggest local blowing snow events at Amundsen Gulf on 13 and 14 March but not on 16 March. The MERRA blowing snow occurrences are mainly driven by the wind speed, which was higher on 13–14 March than 16 March at this location. MERRA data suggest that a wider and stronger region of blowing snow occurred over the north Beaufort Sea on 12–14 March and dissipated on 15 March. The presence of this blowing snow event was confirmed by CALIOP (see Figure S10 in the supporting information). Considering possible transport with recycling of inorganic bromine on blowing snow particles and aerosols, and the high blowing snow flux over the north Beaufort Sea on 12–14 March, an alternative explanation of the morphology of this event is that it was initiated by blowing snow and also diminished as the blowing snow flux dissipated, as discussed above.

Figure 10 displays box and whisker plots for column-integrated mass of GEOS-5 blowing snow SSA, wind speed at 10 m, and temperature at 10 m during this period, similar to Figure 8. We note that the range of SSA column mass is much lower than for other cases presented in this study. Overall, tropospheric column BrO and blowing snow SSA do not exhibit a substantial correlation ($r = 0.24$). This low correlation may result from model uncertainties. The correlation coefficient between wind speed at 10 m and OMI tropospheric column BrO is 0, and that between temperature at 10 m and OMI tropospheric column is −0.25. Both correlation coefficients are lower than that between GEOS-5 blowing snow SSA and OMI tropospheric column BrO.

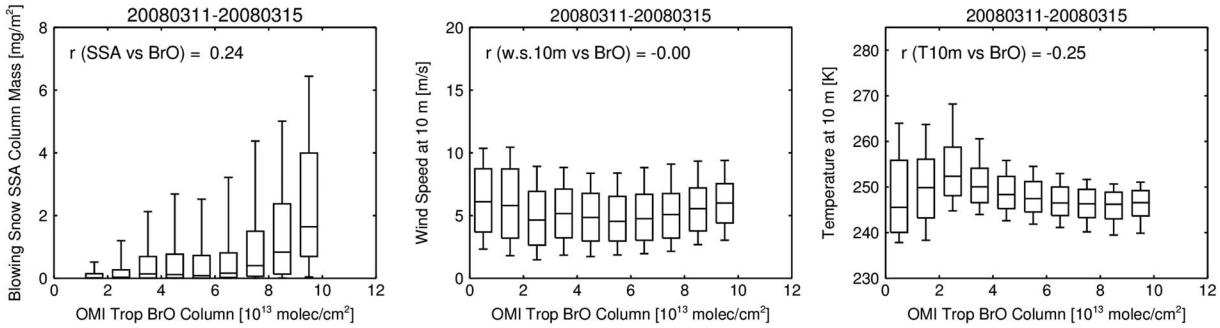

Figure 10. Similar to Figure 8 but for box and whisker plots showing 10th, 25th, median, 75th, and 90th percentiles for (a) Goddard Earth Observing System-5 simulated blowing snow-generated SSA, (b) wind speed at 10 m, and (c) temperature at 10 m, as a function of OMI-observed tropospheric column BrO, for each 1×10^{13} molecule/cm^2 step of BrO column during 11–15 March 2008. All data poleward of 65°N are used to obtain the correlation coefficients, while box and whisker plots show bins only where the numbers of data points are greater than 1% of the total number of data points. SSA = sea-salt aerosol; OMI = Ozone Monitoring Instrument.

We note that this particular case is associated with a high-pressure system (not shown). The high wind speeds that trigger blowing snow events are usually associated with large pressure gradients. Since pressure gradients can be associated with high- and low-pressure systems, blowing snow events can also occur near both. Although many studies have reported BrO explosions that coincide with low-pressure systems and subsequent bad weather (e.g., Begoin et al., 2010; Blechschmidt et al., 2015; Choi et al., 2012), here we show that high-pressure systems can also be associated with BrO explosions.

3.3.3. The 1–5 April 2008 Event

Here we examine an event that occurred near the north coast of Siberia and the North Pole in early April 2008. Figure 11 shows maps of GEOS-5 column-integrated blowing snow SSA and OMI tropospheric column for 1–5 April 2008. On 1 April 2008, a region of high blowing snow SSA occurred at the north coast of Siberia and a structure of enhanced tropospheric column BrO coincides with this region. During 2–4 April 2008, a structure of high blowing snow SSA developed near 90°E, 85°N, where a structure of high tropospheric column BrO also appeared. During 4–5 April 2008, this blowing snow SSA structure split in two, and the high tropospheric BrO structure showed a similar spatial pattern. We also see structures of high blowing snow SSA and tropospheric column BrO over the Bering Strait on 5 April 2008.

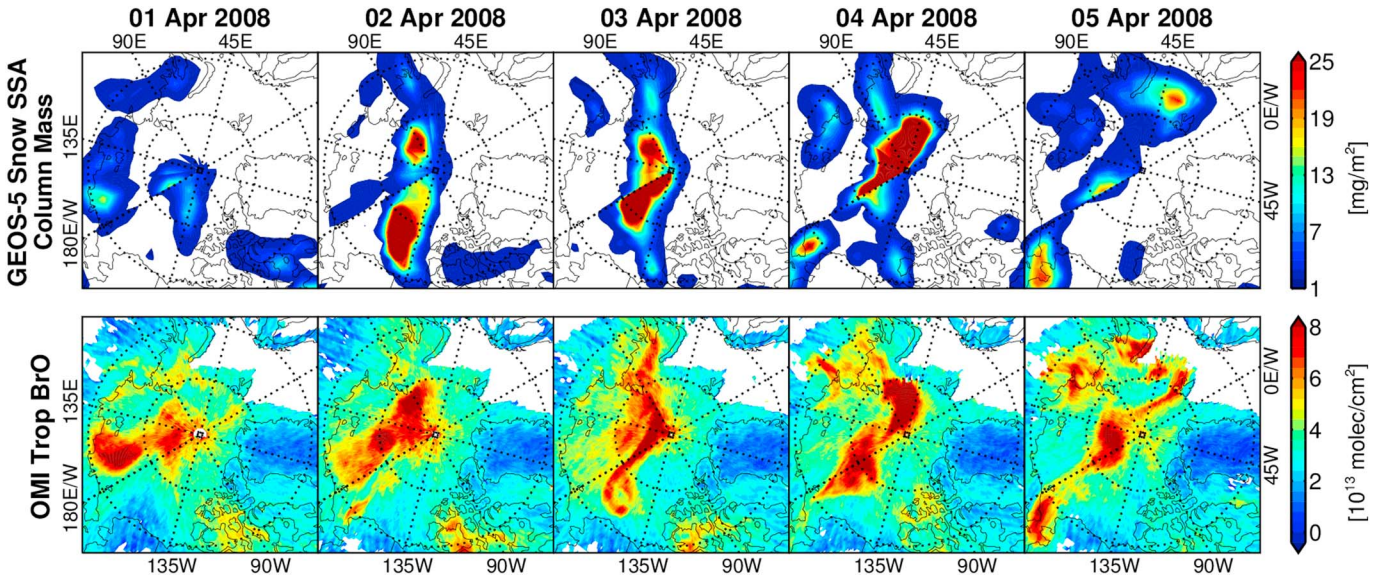

Figure 11. Similar to Figure 7 but for (top) Column-integrated mass of blowing snow-generated SSAs simulated using GEOS-5, (bottom) OMI-observed tropospheric column BrO for 1–5 April 2008. For top panels, regions for which OMI tropospheric column did not pass the filtering criteria (see the last paragraph of section 2.1.3) are denoted as white. For bottom panels, regions where SSA column mass < 1 mg/m^2 are denoted using white. GEOS = Goddard Earth Observing System; SSA = sea-salt aerosol; OMI = Ozone Monitoring Instrument.

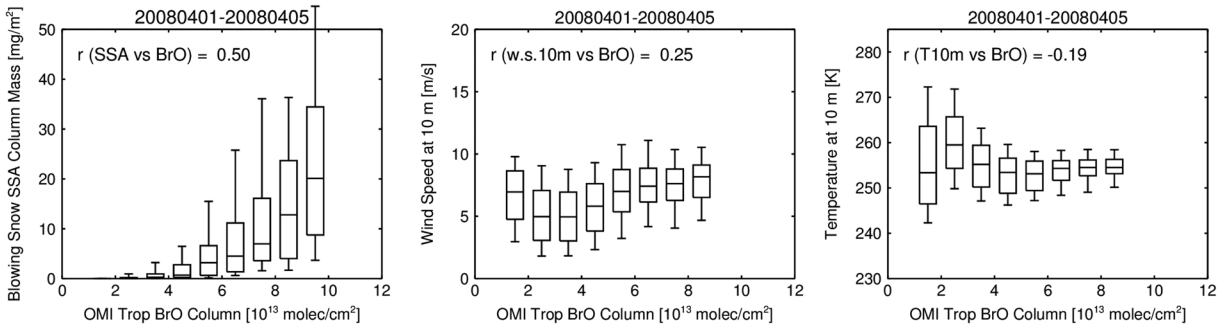

Figure 12. Similar to Figure 8, Box and whisker plots showing 10th, 25th, median, 75th, and 90th percentiles for (a) Goddard Earth Observing System-5 simulated blowing snow-generated SSA, (b) wind speed at 10 m, and (c) temperature at 10 m, as a function of OMI-observed tropospheric column BrO, for each 1×10^{13}-molecules/cm^2 step of BrO column during 1–5 April 2008. All data poleward of 65°N are used to obtain the correlation coefficients, while box and whisker plots show bins only where the numbers of data points are greater than 1% of the total number of data points. SSA = sea-salt aerosol; OMI = Ozone Monitoring Instrument.

We note a discrepancy between blowing snow SSA and tropospheric column BrO at the north coast of Alaska on 2 April 2008, where we compute a high amount of SSA column mass, while no enhancement of tropospheric BrO was observed. This result may be explained by the presence of multiple-year sea ice over this region (see Figure S11b), snow on which would be less saline than that on first-year sea ice (Krnavek et al., 2012) and thus emit little blowing snow SSA mass flux.

Figure 12 shows a box and whisker plot for column-integrated mass of GEOS-5 blowing snow SSA and OMI tropospheric column BrO accompanied by the correlation coefficient between the two quantities, similar to Figure 8. The two quantities exhibit overall reasonably good correlation. The slightly lower correlation coefficient ($r = 0.50$) than found for the event during 24–29 March 2007 may be due to the disagreement of high SSA but low tropospheric BrO, explained in the previous paragraph, on 2 April 2008. The correlation coefficient between wind speed at 10 m and OMI tropospheric column BrO is 0.25, and that between temperature at 10 m and OMI tropospheric column is −0.19. As in the previous case studies, both correlation coefficients are lower than that between GEOS-5 blowing snow SSA and OMI tropospheric column BrO.

3.3.4. The 15–19 April 2008 Event

We examine an event that occurred near the North Pole and Chukchi Sea during 15–19 April 2008. Since this event overlapped with two aircraft missions, NASA ARCTAS and NOAA ARCPAC, tropospheric BrO explosions that occurred during this period have been investigated in previous studies, which reported the presence of high tropospheric active bromine species from aircraft in situ measurements (Choi et al., 2012; Liao, Huey, Scheuer, et al., 2012; Neuman et al., 2010; Salawitch et al., 2010). We extend these analyses by including the GEOS-5 simulated blowing snow SSA.

Figure 13 shows maps of column-integrated mass of GEOS-5 blowing snow SSA and OMI tropospheric column BrO for 15–19 April 2008. Near the North Pole, a structure of high blowing snow SSA appeared during 16–18 April 2008 and gradually diminished on and after 19 April 2008. OMI observations also report high tropospheric column BrO over this area. We note that aircraft in situ measurements during NASA ARCTAS confirm high tropospheric BrO mixing ratios in this region (Choi et al., 2012; Liao, Huey, Scheuer, et al., 2012; Salawitch et al., 2010). On 19 April 2008, a crescent-shaped structure of high blowing snow SSA appeared in the Chukchi Sea, and this structure overlaps exactly where OMI observations also reported enhanced tropospheric column BrO. The presence of large amounts of active bromine (Br_2 + HOBr > 6 pptv) has been reported by Neuman et al. (2010; see Figure 1 of Neuman et al., 2010, and Figure 15 in section 3.3.5). We also see additional small regions of high blowing snow SSA and enhanced tropospheric column BrO where aircraft measurements are not available, such as the north coast of Alaska, United States, during 15–16 April 2008 and the Canadian Archipelago on 19 April 2008.

The correlation between column-integrated mass of GEOS-5 simulated blowing snow SSA and OMI tropospheric column BrO is summarized in Figure 14. Column-integrated mass of GEOS-5 blowing snow SSA and OMI tropospheric column BrO exhibit a reasonably good correlation during this period ($r = 0.56$). The correlation coefficient of wind speed at 10 m and OMI tropospheric column BrO is 0.04. Finally, the correlation coefficient of temperature at 10 m and OMI tropospheric column BrO is 0.11.

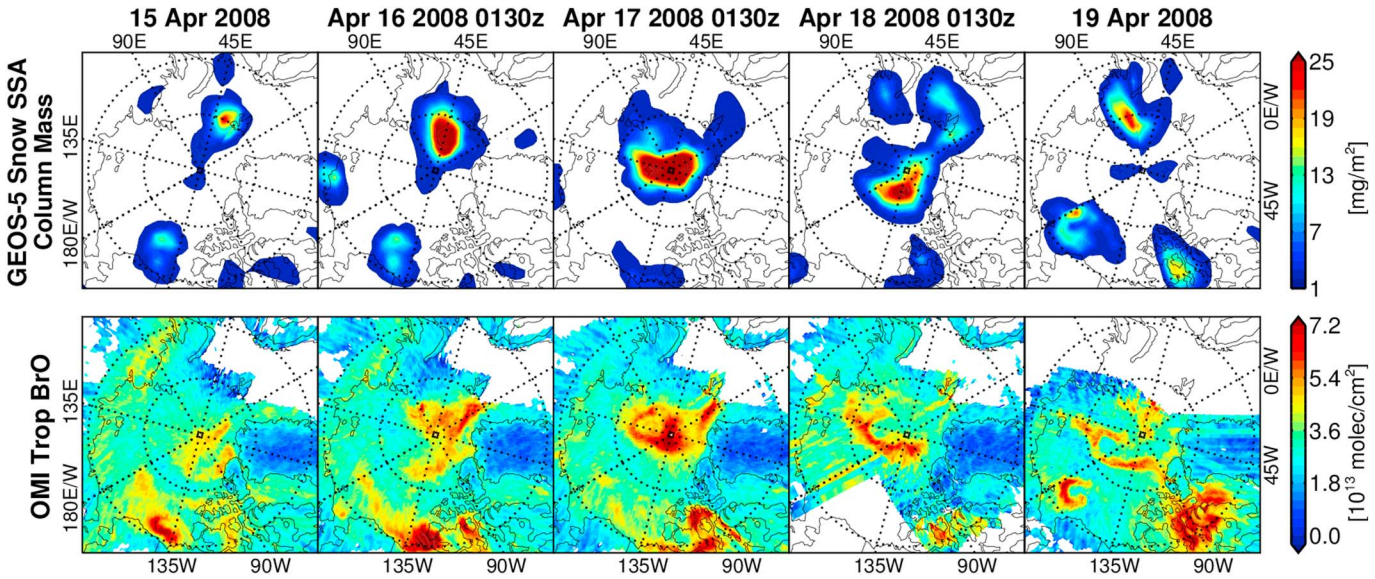

Figure 13. Similar to Figure 7 but for (top) column-integrated mass of blowing snow-generated SSAs simulated using GEOS-5, (bottom) OMI-observed tropospheric column BrO but for 15–19 April 2008. For top panels, regions for which OMI tropospheric column did not pass the filtering criteria (see the last paragraph of section 2.1.3) are denoted as white. For bottom panels, regions where SSA column mass <1 mg/m^2 are denoted using white. GEOS = Goddard Earth Observing System; SSA = sea-salt aerosol; OMI = Ozone Monitoring Instrument.

3.3.5. Discussion of the Case Studies

The case studies presented here indicate that the spatial patterns of BrO explosions are similar to those of blowing snow-generated SSAs. We note that locations of OMI-observed high BrO do not necessarily spatially overlap with the place of the GEOS-5 simulated blowing snow SSA emission. We have performed correlation analysis of tropospheric column BrO versus temperature and wind speed but find little correlation, while BrO and blowing snow SSA exhibit moderate correlation in most of our case studies (Figures 8, 10, 12, and 14). These results indicate that it is blowing snow-generated SSA (driven by meteorological factors such as high wind speed) that is associated with tropospheric BrO explosions, rather than mere meteorological factors. However, these results do not discount possible connections of BrO explosion events to wind speed or temperature. In fact, effects of wind speed and temperature are already reflected in blowing snow "emission flux," where simulated SSA is based on this emission. Although we do not find direct correlation between wind speed (or temperature) and the BrO column over the entire Arctic poleward of 65°N, the correlation found between the blowing snow SSA and BrO column shows the indirect connection of wind speed and temperature to the observed BrO explosion events.

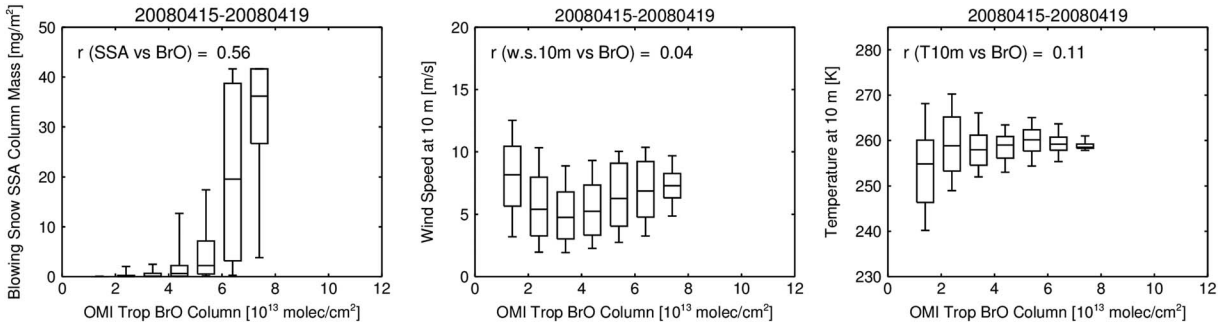

Figure 14. Similar to Figure 8 but for box and whisker plots showing 10th, 25th, median, 75th, and 90th percentiles for (a) Goddard Earth Observing System-5 simulated blowing snow-generated SSA, (b) wind speed at 10 m, and (c) temperature at 10 m, as a function of OMI-observed tropospheric column BrO, for each 1 × 10^{13}-molecules/cm^2 step of BrO column during 15–19 April 2008. All data poleward of 65°N are used to obtain correlation coefficients, while box and whisker plots show bins only where the numbers of data points are greater than 1% of the total number of data points. SSA = sea-salt aerosol; OMI = Ozone Monitoring Instrument.

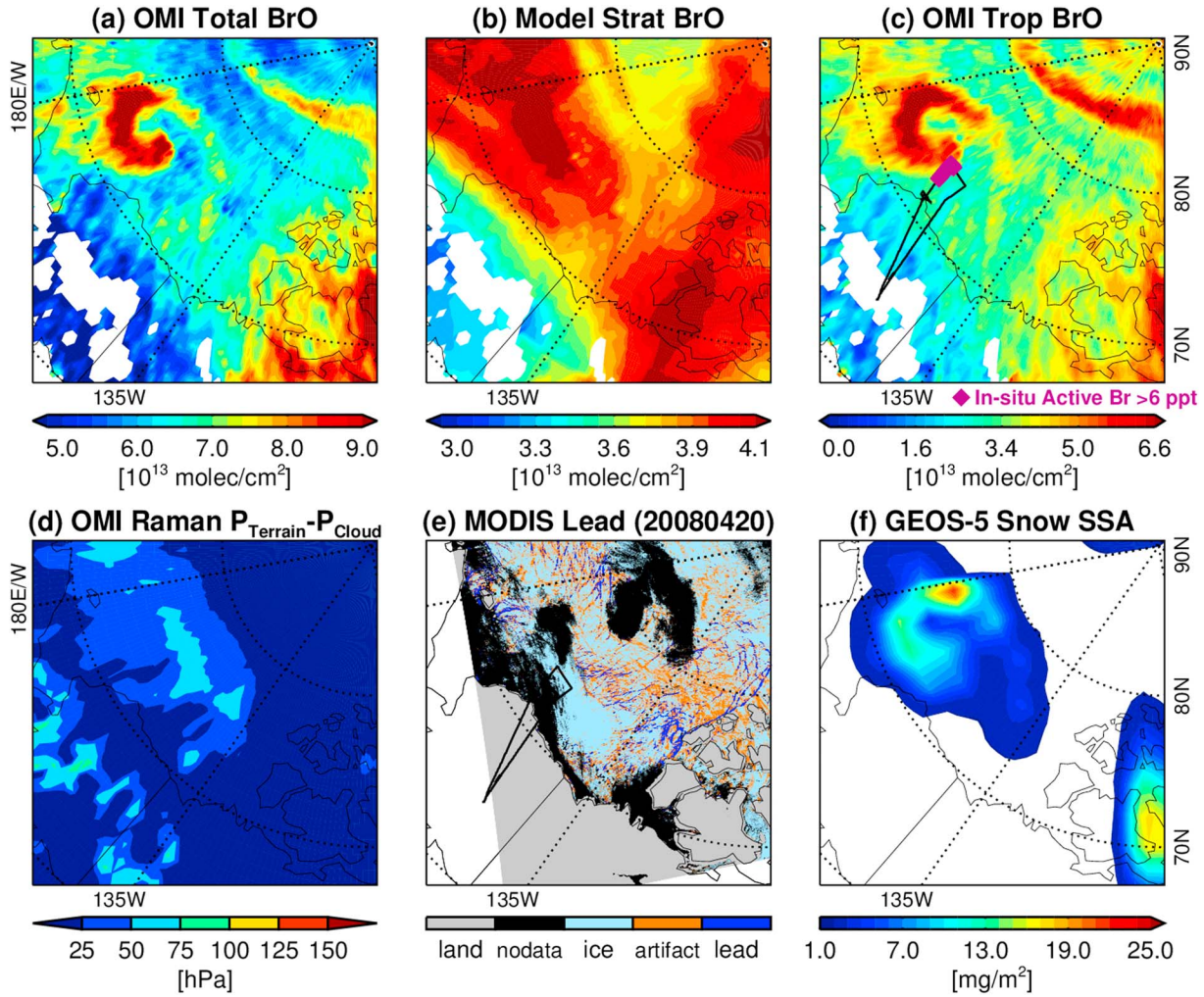

Figure 15. (a) OMI total column BrO, (b) model-estimated stratospheric column BrO, (c) OMI tropospheric column BrO, (d) terrain pressure minus OMI Raman cloud pressure ($P_{Terrain} - P_{Cloud}$) of where the BrO columns are sampled, (e) MODIS sea ice lead measurements (on 20 April 2008), and (f) column-integrated mass of GEOS-5 simulated blowing snow sea-salt aerosol. Maps are for 19 April 2008 except for panel (e), because cloud conditions obscured the MODIS view of leads on 19 April 2008. In panels (c) and (e), the flight track by Neuman et al. (2010) is shown in black lines. In panel (c), the locations where aircraft measurements by Neuman et al. (2010) report the presence of a large amount of active bromine (>6 pptv) are marked (purple). For panels (a) to (c), regions for which OMI tropospheric column did not pass the filtering criteria (see the last paragraph of section 2.1.3) are denoted as white. For panel (d), regions for without the OMI Raman cloud data are denoted using white. For panel (e), regions without MODIS lead data are denoted as white, land surfaces are denoted using gray, while regions obscured by clouds are denoted with black. For panel (f), regions with sea-salt aerosol mass less than 1 mg/m^2 are denoted as white. OMI = Ozone Monitoring Instrument; MODIS = Moderate Resolution Imaging Spectroradiometer; GEOS = Goddard Earth Observing System.

In the case study in section 3.3.3, a part of the discrepancy between GEOS-5 SSA and OMI BrO column might be due to our assumptions for snow salinity. On 2 April 2008 (Figure 11), the GEOS-5 model simulates high blowing snow SSA at the north coast of Alaska, United States, while the OMI BrO column is low in this region. Sea ice age in this area is equal to or older than 2 years (see Figure S11b). This type of disagreement (i.e., high SSA without a tropospheric BrO enhancement) may be explained by the presence of multiple-year sea ice (and thus lack of first-year sea ice). According to Krnavek et al. (2012), salinity on multiple-year sea ice is much lower than that of first-year sea ice, which may cause reduced blowing snow SSA mass emission flux over this type of surface (see section 2.2). However, the presence of multiple-year sea ice does not explain all cases of high SSA that do not coincided with high BrO in other case studies. For instance, we see a case of large amount of SSA without corresponding BrO enhancement at the north coast of Russia on 15 March 2008, (Figure 9 in section 3.3.2) but the sea ice in this region was mostly first-year sea ice (see Figure S11a). An explanation of this type of discrepancy is the possible presence of bromide-depleted SSA.

Our analysis is focused on blowing snow as a source of SSA over sea ice, rather than leads. While studies show that increased cloud condensation nuclei (Leck et al., 2002) and SSA (May et al., 2016) are associated with leads, our analysis is focused on regions of elevated tropospheric BrO over sea ice/snow surfaces that are below the temperature at which open water would be present. Most importantly, the NOAA WP-3D aircraft extensively sampled BrO over leads in the Arctic during ARCPAC (Neuman et al., 2010). They saw little or no enhancements of active bromine and suppression of O_3 for these low-altitude flight legs. Conversely, on 19 April 2008, the WP-3D measured high concentrations of active bromine in precisely the same area as revealed by our tropospheric residual BrO product (Figure 15).

Next, the relation of OMI tropospheric BrO to sea ice leads is further explored. Figure 15 shows OMI measurements of total column BrO, model-based stratospheric column BrO, OMI tropospheric column BrO, terrain pressure minus the OMI Raman cloud pressure ($P_{Terrain} - P_{Cloud}$), where the BrO columns are sampled, MODIS Arctic sea ice lead map, and column mass of GEOS-5 blowing snow SSA. The flight track of the NOAA WP-3D aircraft on 19 April 2008 is shown in panels (c) and (e). The aircraft measured the presence of a large amount of active bromine (>6 pptv) on this date, at the region denoted using purple on panel (c). All maps shown in Figure 15 are for 19 April 2008, except for the MODIS sea ice lead map, which is for 20 April 2008. Unfortunately, cloudy conditions obscured the view of the surface by MODIS thermal infrared measurements on 19 April 2008. However, the enhancement of tropospheric column BrO over the bright surface (i.e., snow and ice) is observed even in the presence of these clouds. The OMI Raman cloud product is able to distinguish the presence of optically thick clouds that shield the surface below from UV measurements. This product (Figure 15d) shows that shielding clouds (detected when $P_{Terrain} - P_{Cloud}$ is greater than 100 hPa) were not present in the vicinity of the observed bromine enhancement on 19 April 2008.

The locations at which elevated active bromine was measured by the NOAA WP-3D aircraft on 19 April 2008 lie close to a plume of elevated tropospheric column BrO revealed by our analysis of OMI data (Figure 15c). There is close correspondence between this plume of OMI tropospheric BrO and the mass blowing snow SSA simulated by GEOS-5. The MODIS product indicates the absence of leads directly below the aircraft. However, MODIS did detect the presence of numerous "artifacts," that is, 50% chance of true leads upwind of the regions where elevated active bromine was measured. The correspondence between the locations of the BrO explosions observed by OMI and the GEOS-5 SSA product, as well as the lack of OMI observation of elevated BrO over regions of leads recorded by MODIS (e.g., 75°N, 125°W, around the northwest edge of Banks Island), suggests that the blowing snow is more strongly related to active bromine observed on 19 April 2008 than sea ice leads. Because SSA can also be produced from leads (Leck et al., 2002; May et al., 2016) and subsequently be transported downwind of this source, however, we cannot rule out the contribution of leads to bromine activation based solely on the lack of spatial correlation between leads and high BrO. Furthermore, the low albedo of open water (leads) also reduces the near-surface sensitivity of OMI BrO as compared to snow or ice covered surfaces that have higher reflectivity. Rather, the enhanced tropospheric BrO that was observed by OMI exhibits high spatial and temporal correlations with SSA generated by blowing snow.

The supply of BrO can be limited by the availability of ozone. Ozone is necessary for production of BrO (see equation (3) and also Choi et al., 2012) and may become depleted in the catalytic cycle within a shallow mixing layer, which is commonly associated with a low PBL height. In favorable conditions (i.e., high PBL height), either at the site of a blowing snow event or after transport, a catalytic "explosion" may occur in which a high tropospheric BrO column appears. Zhao et al. (2016) reported long-range transport of tropospheric BrO explosion from Beaufort Sea to Eureka using back trajectory analysis, where meteorological data exhibit strong wind speed (24 m/s) and elevated boundary layer height (~800 m) at Beaufort Sea.

In Figure 16, we present a correlation analysis supporting the importance of PBL height in BrO explosion events on a local scale. Figures 16a and 16b illustrates OMI tropospheric column BrO and MERRA PBL height for 12–14 March 2008. We note that the spatial patterns of enhanced BrO column and high PBL height are similar at a local scale. Figure 16c presents a box and whisker plot and the correlation coefficient between these two variables, sampled in the area shown in panels (a) and (b), to provide a quantitative view of their relationship. Tropospheric BrO column and PBL height exhibit a moderate correlation coefficient ($r = 0.5$) at this local scale (which corresponds to a well-defined BrO explosion event), while no significant correlation between these two quantities is observed over the entire Arctic area (e.g., region poleward of 65°N).

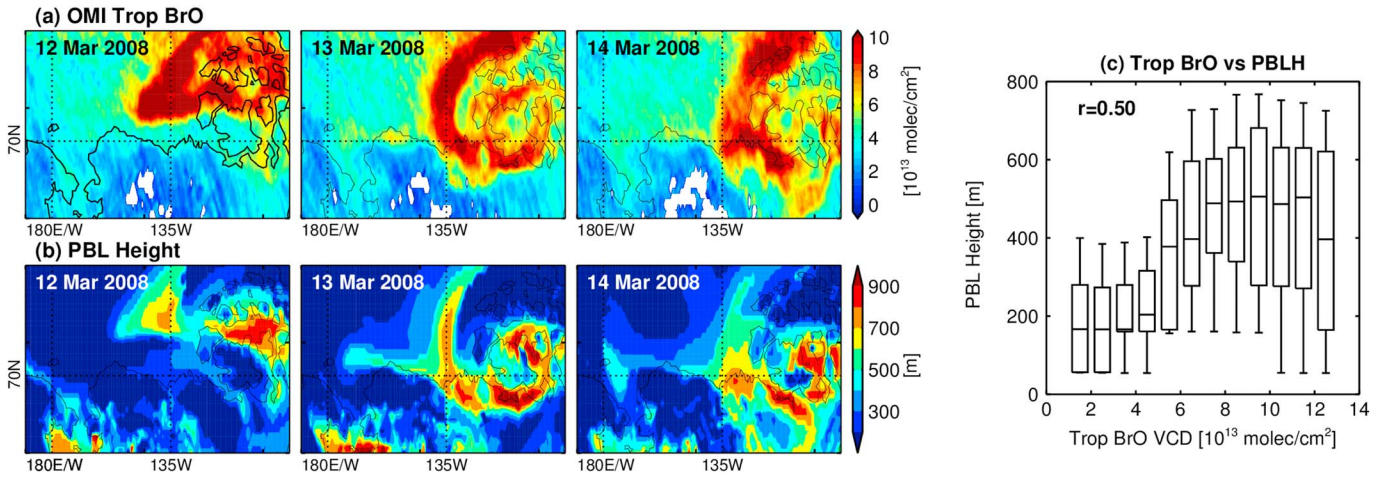

Figure 16. For 12–14 March 2008, (a) OMI tropospheric column BrO, (b) Modern-Era Retrospective Analysis for Research and Applications PBL height, and (c) a box and whisker plot with the correlation coefficient between these two variables sampled in the plotted area. For panel (a), regions for which OMI tropospheric column did not pass the filtering criteria (see the last paragraph of section 2.1.3) are denoted as white. For panel (c), the box and whisker plot shows bins only where the numbers of data points are greater than 1% of the total number of data points. OMI = Ozone Monitoring Instrument; PBLH = planetary boundary layer height; VCD = vertical column density.

Moreover, Figure 16c implies the presence of two groups of data; suppressed PBL (median $\lesssim$200 m) with low to moderate BrO ($VCD_{Trop} \lesssim 5 \times 10^{13}$ molecules/cm^2) and elevated PBL (median $\gtrsim$500 m) with enhanced BrO ($VCD_{Trop} \gtrsim 7 \times 10^{13}$ molecules/cm^2).

Our analysis indicates that observations of elevated tropospheric column BrO can be associated with a deep boundary layer. However, this result does not rule out the possible presence of high mixing ratios of BrO within a shallow boundary layer. When this condition does occur, the contribution of enhanced BrO to the tropospheric column tends to be modest. For example, to obtain VCD_{Trop} of 6×10^{13} molecules/cm^2 for a temperature of 250 K in a shallow boundary layer with a height of 200 m requires a BrO mixing ratio of ~100 pptv, assuming that BrO is uniformly mixed. Ground-based measurement studies generally report maximum BrO mixing ratio of several tens of pptv. Sihler et al. (2012) reported a BrO maximum of 40 pptv in the Amundsen Gulf near Canadian Archipelago during March 2008, which is an extremely high value. Therefore, the contribution of elevated BrO in shallow boundary layer events to BrO explosions observed from space is not likely to be significant.

Finally, we mention a challenge faced in this and similar studies. Low-pressure systems that produce blowing snow events may be associated with a low-altitude tropopause and thus high stratospheric BrO columns (Salawitch et al., 2010). However, many of the features we detect as tropospheric enhancements have spatial scales much smaller than those of high stratospheric columns (e.g., see Figure 2). This provides confidence that our detection of tropospheric BrO enhancements is robust.

3.4. Interannual Variability

Here we show the correlation between observed tropospheric BrO explosion frequency and the simulated blowing snow-generated SSA emission flux. Also, we extend the analysis to nearly the entire time period of OMI observation (2005–2015) by using blowing snow-generated SSA emission flux. Although the emission flux may be spatially offset from the location of the blowing snow-generated SSA, we nonetheless use time series of the emission flux, rather than simulated snow blown SSA, because the latter is only available for a few case studies due to the computational challenges. Furthermore, the time series analysis relies on analysis of the frequency of various events and not the precise matching of geolocation.

We investigate the relationship between the OMI tropospheric BrO explosion frequency and the blowing snow SSA emission flux during March and April, for years 2005 to 2015, at latitudes >65°N. The BrO explosion frequency is quantified using the area-weighted fraction of gridded OMI tropospheric BrO VCD where tropospheric BrO VCD $>6 \times 10^{13}$ molecules/cm^2, approximately the top 5th percentile. For this analysis, we use BrO explosion frequency count and SSA emission flux obtained for the entire area of interest (latitude >65°N).

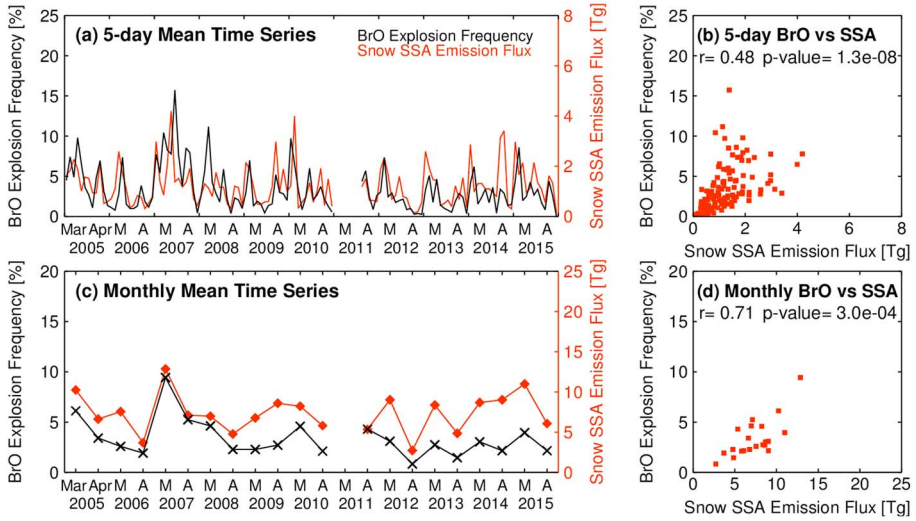

Figure 17. Time series and correlation analysis during March and April for 2005–2015; (a) 5-day average time series of BrO explosion frequency (black) and blowing snow SSA total emission flux per each 5-day period (red), (b) scatter plot between 5-day average BrO explosion frequency and blowing snow SSA emission flux, (c) and (d), similar to (a) and (b), respectively, but in monthly temporal resolution. Note that the March 2011 data are excluded in time series analysis as stated in section 2.1.2. SSA = sea-salt aerosol.

We note that the March 2011 data are excluded in the time series analysis because they are affected by low stratospheric ozone in the Arctic, as stated in section 2.1.2.

Figure 17a shows the 5-day average time series of BrO explosion frequency (black) and SSA emission flux (red) during March and April for years 2005 to 2015, and Figure 17b presents the correlation analysis of BrO explosion frequency and blowing snow SSA emission flux during the given period. The 5-day time series during the 11 years shows that a number of peaks in the BrO explosion frequency coincide with large amounts of blowing snow SSA emission, although the 11-year correlation analysis of the 5-day time series indicates only moderate correlation ($r = 0.48$). We note that the time series with reduced temporal resolution (≥10 days) shows a higher correlation ($r \gtrsim 0.68$) between the frequency of occurrence of BrO explosions and SSA emission (see Figures S12a–S12d in the supporting information).

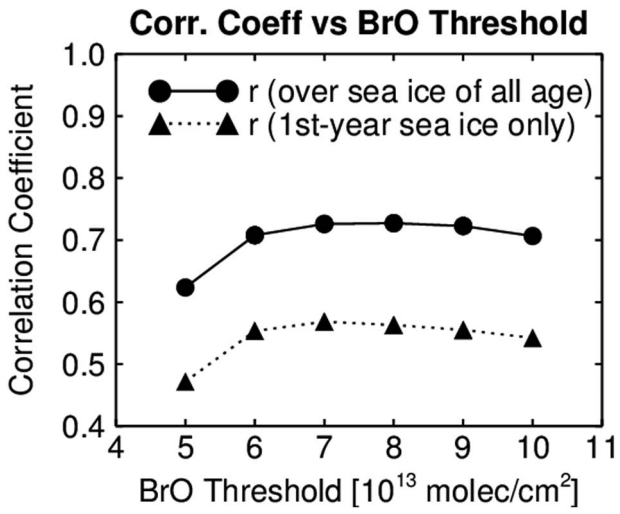

Figure 18. Correlation coefficient between monthly time series of tropospheric BrO explosion frequency and blowing snow-generated sea-salt aerosol (SSA) emission flux, as a function of thresholds used to define tropospheric BrO explosion assuming; (solid line) blowing snow SSA emission over sea ice of any age and (dot line) blowing snow SSA emission over first-year sea ice only.

Figures 17c and 17d show similar time series and scatter plots to Figures 17a and 17b but with a lower temporal resolution (monthly). Monthly average BrO explosion frequency and blowing snow SSA emission flux exhibit a reasonable correlation ($r = 0.71$), explaining ~50% of the variance in BrO explosion frequency. Even with the reduced number of data points, the p value is low (3.0×10^{-4}) implying statistical significance of the correlation between high BrO and blowing snow occurrence. This correlation is partly driven by differences for data collected in March and April; both the blowing snow SSA emission and the BrO explosion events tend to occur more frequently in March than April. The central Arctic region is colder in March, and the stronger temperature gradient between the central Arctic and the Atlantic Ocean produces stronger geostrophic winds, which is the likely cause of more frequent blowing snow events in March. More frequent BrO explosions in March may be a result of higher blowing snow SSA emission flux. Moreover, the similar interannual variability with yearly temporal resolution also exhibits reasonable correlation ($r = 0.70$), which supports the potential connection between Arctic tropospheric BrO explosions and blowing snow-generated SSAs (see Figures S12e and S12f in the supporting information).

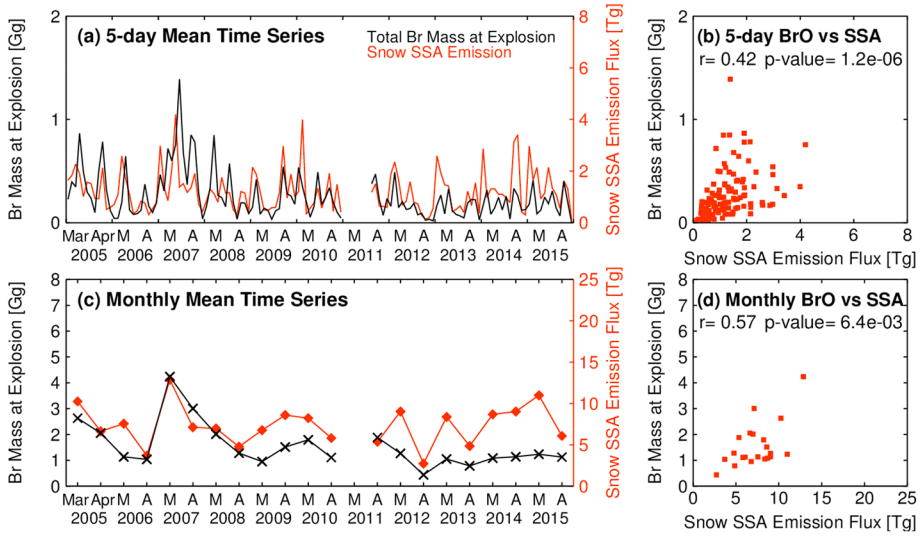

Figure 19. Similar to Figure 17 but using mass of bromine computed from the Ozone Monitoring Instrument observations, summed over the area where the tropospheric BrO explosion occurs (i.e., tropospheric column BrO $>6 \times 10^{13}$ molecules/cm^2). SSA = sea-salt aerosol.

We note that the correlation between tropospheric BrO explosion frequency and blowing snow-generated SSA emission flux is robust regardless of how the threshold is defined. The correlation coefficient ranges between 0.6 and 0.7 when the threshold is varied between 5×10^{13} and 10×10^{13} molecules/cm^2 (solid line in Figure 18).

In Figure 19, we also analyze the time series of BrO explosion in terms of mass of bromine (units of gigagram) computed from the satellite observations, summed over the area where the tropospheric BrO explosion occurs. The correlation between the mass of bromine and SSA emission flux is present, at a level close to the one found using frequency, though a bit lower ($r = 0.42$ in 5-day temporal resolution and 0.57 in the monthly time series).

First-year sea ice has also been suggested to be associated with active bromine species and/or BrO explosions (Nghiem et al., 2012; Simpson et al., 2007). However, these two studies do not completely rule out the possible connection between the observed high BrO column and particles generated from blowing snow.

We also test the assumption that blowing snow SSA emission occurs only over first-year sea ice. The correlation between BrO explosion frequency and SSA emission flux only over first-year sea ice is lower than the correlation found using SSA emission over all sea ice (Figure S13 in the supporting information). For example, the correlation coefficient of the monthly time series of SSA emission flux over only first-year sea ice is 0.55 (Figure S13f), while that of SSA emission flux over all sea ice is 0.71 (Figure 17d). Larger correlations are found using SSA emission over all sea ice compared to correlations for first-year sea ice upon use of 5-day temporal resolution (Figures 17b and S13b), as well as 10-day and yearly resolutions (Figures S12 and S13). Correlation coefficients found using various BrO thresholds are summarized in Figure 18 (dotted line), showing consistently higher correlation for emission over all sea ice than found for emission only over first-year sea ice. Our analysis suggests that first-year sea ice could be an important source of SSA generated by blowing snow but is likely not the sole source.

In Figure 20, we show a time series of the estimated first-year ice area using the Arctic Sea Ice Index along with the BrO explosion frequency (Figure 20a) and the associated scatter plot (Figure 20b) between them. The first-year sea ice area shows a rapid increase in the spring of 2008, reflecting the drastic Arctic sea ice decline in the summer of 2007 (Maslanik et al., 2007; Nghiem et al., 2007; Perovich et al., 2008; Richter-Menge et al., 2008). The correlation between BrO explosion frequency and seasonal sea ice area, however, is low ($r = -0.35$) for the overall time series. First-year sea ice and the frequency of BrO explosions do not exhibit a statistically significant correlation, despite the fact that seasonal (first-year) sea ice area is usually greater in March than in April. This lack of correlation between BrO and first-year sea ice actually supports the notion that the correlation between BrO and blowing snow is not merely the result of the March–April variations.

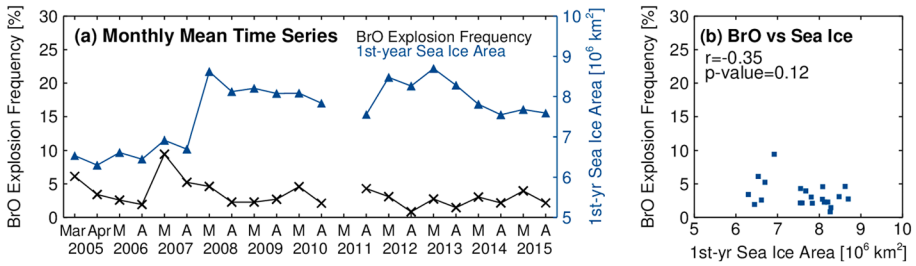

Figure 20. Time series and correlation analysis during March and April for 2005–2015; (a) Monthly average time series of BrO explosion frequency (black) and first-year sea ice area (blue) and (b) scatter plot between monthly average BrO explosion frequency and first-year sea ice area.

Moreover, the yearly time series analysis does not exhibit significant correlation between the BrO explosion frequency and the first-year sea ice area ($r = -0.56$, see Figure S14 in the supporting information). This suggests that the BrO explosion frequency is driven mainly by meteorology (wind speed is a key factor for blowing snow events) as opposed to first-year sea ice, an alternate source of active bromine.

3.5. Additional Caveats

Here we mention some potential limitations of our analysis. Areas close to the North Pole are not included in most periods of March because of the high SZA and the consequent impact on the measurement of BrO. The lack of polar coverage is unfortunate, since high winds and the potential for enhanced BrO exist near the pole in March for certain days, including several illustrated in Figure 9. This problem is more acute for early March; by the end of March (i.e., Figure 7), coverage is nearly complete and the loss of measurements at the pole has no impact on the interpretation of enhanced BrO.

We note that the discrepancy between OMI tropospheric BrO VCD and MERRA-driven SSA emission flux may result from the fact that the blowing snow SSA flux is obtained only over the sea ice.

More than one third of the pixels from OMI were neglected after April 2008 owing to the row anomaly. We conducted the same analysis using only the data from OMI rows 0–20 (not affected by the row anomaly) in every year. This provides results similar to those obtained with the data from all good rows (i.e., different numbers of rows used in different years; see Figures S15 and S16 in the supporting information).

We hypothesize that blowing snow events cause emission of SSA, but we note that blowing snow and SSA are not synonymous. While Frieß et al. (2011) reported that elevated concentrations of BrO occurred mainly in the presence of high aerosol extinction with strong winds near the surface, there were no measurements of the chemical composition of the aerosol to show that SSA was responsible for the observed high extinction values.

Finally, Rhodes et al. (2017) reported observations of salinity of snow particles entrained from sea ice during blowing snow events in the Weddell Sea, Antarctica, that had a mean salinity of 0.30 psu. This value of salinity is about 14 times smaller than the mean value from Antarctica reported by Massom et al. (2001), which we have used in our model. Rhodes et al. (2017) do not report a PDF of salinity and they state "any individual salinity measurements >10 psu are excluded." This exclusion is important, because salinities above 10 psu can occur. Massom et al. (2001) state "as a result of capillary suction of brine, high salinities (>10 psu) occur up to about 0.1 m in the snow column but mainly in the 0.00–0.05-m layer (Massom et al., 1997, 1998), as shown in their Figure 11." As such, we place greater emphasis on the Massom et al. (2001) estimate of salinity, since their PDF is inclusive of all measurements. Even if the true Arctic snow salinity is closer to Rhodes et al. (2017) than Massom et al. (2001), the reduced salinity will lower the SSA mass emission flux but will not change the conclusion derived based on the higher salinity as the correlation coefficient between modeled SSA and OMI BrO measurements will not change significantly.

4. Conclusions

We have investigated the potential link between Arctic tropospheric BrO explosions and SSAs generated from blowing snow events using OMI tropospheric column BrO and the GEOS-5 model. The GEOS-5 model, driven by the MERRA meteorological reanalysis, is used to quantify the amount of blowing snow-generated

SSAs. The primary factor needed to produce blowing snow-generated SSAs is high wind speed that is typically driven by large pressure gradients. Blowing snow events can occur near both high- and low-pressure systems, provided that the pressure gradient is sufficient to generate winds that exceed the threshold value for blowing snow. The simulated blowing snow-generated SSA emission flux results in higher emission in March than in April. This difference is likely due to stronger geostrophic winds in March, which are driven by the higher-temperature gradient (between midlatitudes and polar regions) in March than in April (Serreze et al., 1997). Of course, the Arctic tends to be colder in March than in April, due to seasonal variations in solar exposure.

We have conducted case studies for four BrO explosion events that occurred in spring 2007 and 2008. Tropospheric column BrO from OMI, the simulated blowing snow-generated SSAs, and MERRA meteorological fields suggest that the observed BrO explosion events occurred at locations with large amount of SSAs. The case study of the March 2008 event suggests possible transport of inorganic bromine, associated with recycling of inorganic bromine through snow or aerosol particles. We note that the presence of multiple-year sea ice (and thus lack of first-year sea ice) may explain the case of high SSA without an enhancement of BrO observed on 2 April 2008 in section 3.3.3, although it does not explain a similar case on 15 March 2008 in section 3.3.2.

We have also performed a time series analysis of BrO explosion frequency in conjunction with the amount of blowing snow-generated SSA emission, as well as first-year sea ice area, for the period of 2005–2015 during the months of March and April. The monthly BrO explosion frequency and blowing snow-generated SSA emission flux in the Arctic have a significant correlation. In addition, more frequent BrO explosions and higher blowing snow SSA emission flux are reported in March. Overall results support the suggestion that the blowing snow-generated SSAs are connected to BrO explosions in Arctic spring. In contrast, the first-year sea ice area does not show significant correlation with the BrO explosion frequency using the derived tropospheric BrO columns in either month. However, we should not overlook the role of first-year sea ice as a venue of saline snow and thus BrO release through blowing snow events as it can explain some cases with large amounts of GEOS-5 simulated SSAs that do not overlap with enhanced tropospheric column BrO. Any future investigation regarding connection between first-year sea ice and tropospheric BrO explosion needs to be carefully interpreted for individual cases.

Our conclusions are contingent upon a number of assumptions that are worthy of further study. For example, our estimate of SSA is based on the assumption that the salinity of snow in the Arctic is similar to that in the Antarctic reported by Massom et al. (2001). Additional measurements of Arctic snow salinity, in particular, probability distribution functions that span a wide range of conditions, are needed. Our attempt to validate the modeled SSA generated by blowing snow is limited by the large uncertainty in CALIOP detections of blowing snow. Further evaluation and eventual validation of the spaceborne detection of blowing snow is needed. Finally, additional measurements of chemical composition of blowing snow, including the ability to characterize various snow types (e.g., Table 1 of Jacobi et al., 2012), is essential.

The most important conclusion of our study is that BrO explosion events appear to be highly dependent on meteorology, mainly wind speeds driven by pressure gradients. These gradients can be associated with the passage of synoptic storm systems within the Arctic basin. Studies of the recent historical conditions in the Arctic generally show a marked positive trend in cyclonic activity (Graham et al., 2017; Rinke et al., 2017). In particular, Rinke et al. (2017) found an average increase of six extreme storm events per decade over the satellite era in the Arctic North Atlantic. These recent trends imply more frequent high-speed winds as well as greater snowfall; both may affect future frequency and extent of blowing snow episodes and thus BrO explosion events. These recent changes in the polar climate call for further investigations of (1) how polar tropospheric bromine chemistry varies in response to climate change and (2) how polar bromine chemistry may impact regions outside of the Arctic (and Antarctic). Global chemistry-climate models with polar bromine chemistry as well as continued satellite observations are essential for these investigations.

Acknowledgments
This work was supported by the NASA IPY, ACMAP, and Aura science team programs as well as the Smithsonian Institution. Part of the research was carried out at the Jet Propulsion Laboratory, California Institute of Technology, under a contract with NASA. The authors are grateful to the NASA GMAO reanalysis processing and GMI teams, the OMI and CALIPSO data processing teams, ARCPAC data processing team, and the NSIDC data processing team for providing data sets used here. We thank Sascha Willmes and Günther Heinemann for MODIS daily pan-Arctic sea ice lead maps. The authors also thank Xin Yang, J. Andy Neuman, and Charles Brock for helpful email exchanges. We are also grateful to the three anonymous reviewer whose reviews improved this paper enormously. The OMI BrO, ozone, and cloud data and MERRA meteorological field data are available from NASA Goddard Earth Sciences Data and Information Services Center (GES DISC; https://disc.gsfc.nasa.gov/). NSIDC weekly sea ice age maps are available from NSIDC webpage (http://nsidc.org/data/NSIDC-0611). MODIS daily pan-Arctic sea ice lead maps are available from their webpage (https://doi.pangaea.de/10.1594/PANGAEA.854411). ARCPAC aircraft measurements are available from their webpabe (https://www.esrl.noaa.gov/csd/projects/arcpac/). The model-estimated stratospheric column BrO data are available from Nicolas Theys at IASB-BIRA (Nicolas.Theys@aeronomie.be), and the ground-based total and stratospheric column measurements at Harestua are available from the Network for the Detection of Atmospheric Composition Change (NDACC) webpage (http://www.ndsc.ncep.noaa.gov/sites/stat_reps/harestua/). Any additional data may be obtained from Sungyeon Choi (email:sungyeon.choi@nasa.gov).

References

Abbatt, J. P. D., Thomas, J. L., Abrahamsson, K., Boxe, C., Granfors, A., Jones, A. E., et al. (2012). Halogen activation via interactions with environmental ice and snow in the polar lower troposphere and other regions. *Atmospheric Chemical Physics*, *12*, 6237–6271. https://doi.org/10.5194/acp-12-6237-2012

Ariya, P. A., Dastoor, A. P., Amyot, M., Schroeder, W. H., Barrie, L., Anlauf, K., et al. (2004). The Arctic: A sink for mercury. *Tellus*, *56B*, 397–403. https://doi.org/10.1111/j.1600-0889.2004.00118.X

Ariya, P. A., Khalizov, A., & Gidas, A. (2002). Reactions of gaseous mercury with atomic and molecular halogens: Kinetics, product studies, and atmospheric implications. *The Journal of Physical Chemistry A*, *106*, 7310–7320. https://doi.org/10.1021/jp020719o

Barrie, L. A., Bottenheim, J. W., Schnell, R. C., Crutzen, P. J., & Rasmussen, R. A. (1988). Ozone destruction and photochemical reactions at polar sunrise in the lower Arctic atmosphere. *Nature*, *334*, 138–141. https://doi.org/10.1038/334138a0

Begoin, M., Richter, A., Weber, M., Kaleschke, L., Tian-Kunze, X., Stohl, A., et al. (2010). Satellite observations of long range transport of a large BrO plume in the Arctic. *Atmospheric Chemical Physics*, *10*, 6515–6526. https://doi.org/10.5194/acp-10-6515-2010

Blechschmidt, A.-M., Richter, A., Burrows, J. P., Kaleschke, L., Strong, K., Theys, N., et al. (2015). An exemplary case of a bromine explosion event linked to cyclone development in the Arctic. *Atmospheric Chemistry and Physics Discuss*, *15*, 24,955–24,993. https://doi.org/10.5194/acpd-15-24955-2015

Breider, T. J., Chipperfield, M. P., Richards, N. A. D., Carslaw, K. S., Mann, G. W., & Spracklen, D. V. (2010). Impact of BrO on dimethylsulfide in the remote marine boundary layer. *Geophysical Research Letters*, *37*, L02807. https://doi.org/10.1029/2009GL040868

Brion, J., Chakir, A., Charbonnier, J., Daumont, D., Parisse, C., & Malicet, J. (1998). Absorption spectra measurements for the ozone molecule in the 350–830 nm region. *Journal of Atmospheric Chemistry*, *30*, 291–299. https://doi.org/10.1023/A:1006036924364

Buchard, V., da Silva, A. M., Colarco, P. R., Darmenov, A., Randles, C. A., Govindaraju, R., et al. (2015). Using the OMI aerosol index and absorption aerosol optical depth to evaluate the NASA MERRA aerosol reanalysis. *Atmospheric Chemical Physics*, *15*, 5743–5760. https://doi.org/10.5194/acp-15-5743-2015

Burd, J. A., Peterson, P. K., Nghiem, S. V., Perovich, D. K., & Simpson, W. R. (2017). Snowmelt onset hinders bromine monoxide heterogeneous recycling in the Arctic. *Journal of Geophysical Research: Atmospheres*, *122*, 8297–8309. https://doi.org/10.1002/2017JD026906

Buys, Z., Brough, N., Huey, L. G., Tanner, D. J., von Glasow, R., & Jones, A. E. (2013). High temporal resolution Br_2, BrCl and BrO observations in coastal Antarctica. *Atmospheric Chemical Physics*, *13*, 1329–1343. https://doi.org/10.5194/acp-13-1329-2013

Chance, K. (1998). Analysis of BrO measurements from the Global Ozone Monitoring Experiment. *Geophysical Research Letters*, *25*, 3335–3338. https://doi.org/10.1029/98GL52359

Chance, K. (2002). OMI Algorithm Theoretical Basis Document Volume IV: OMI Trace Gas Algorithms, Cambridge, MA, USA.

Chin, M., Ginoux, P., Kinne, S., Torres, O., Holben, B. N., Duncan, B. N., et al. (2002). Tropospheric aerosol optical thickness from the GOCART model and comparisons with satellite and Sun photometer measurements. *Journal of the Atmospheric Sciences*, *59*(3), 461–483. https://doi.org/10.1175/1520-0469

Choi, S., Wang, Y., Salawitch, R. J., Canty, T. P., Joiner, J., Zeng, T., et al. (2012). Analysis of satellite-derived Arctic tropospheric BrO columns in conjunction with aircraft measurements during ARCTAS and ARCPAC. *Atmospheric Chemical Physics*, *12*, 1255–1285. https://doi.org/10.5194/acp-12-1255-2012

Claas, J., Braak, R., & Kroon, M. (2010). Row anomaly: Introduction and flagging OMI Science Team Meeting, De Bilt, Netherlands.

Daumont, D., Brion, J., Charbonnier, J., & Malicet, J. (1992). Ozone UV spectroscopy. I. Absorption cross-sections at room temperature. *Journal of Atmospheric Chemistry*, *15*, 145–155. https://doi.org/10.1007/BF00053756

Déry, S., & Yau, M. K. (1999). A bulk blowing snow model. *Boundary-Layer Meteorology*, *93*, 237–251. https://doi.org/10.1023/A:1002065615856

Déry, S., & Yau, M. K. (1999). A climatology of adverse winter-type weather events. *Journal of Geophysical Research*, *104*(D14), 16,657–16,672. https://doi.org/10.1029/1999JD900158

Douglas, T. A., Sturm, M., Simpson, W. R., Brooks, S., Lindberg, S., & Perovich, D. (2005). Elevated mercury measured in snow and frost flowers near Arctic sea ice leads. *Geophysical Research Letters*, *32*, L04502. https://doi.org/10.1029/2004GL022132

Duncan, B. N., Strahan, S. E., Yoshida, Y., Steenrod, S. D., & Livesey, N. (2007). Model study of the cross-tropopause transport of biomass burning pollution. *Atmospheric Chemical Physics*, *7*, 3713–3736. https://doi.org/10.5194/acp-7-3713-2007

Ebinghaus, R., Kock, H. H., Thmme, C., Einax, J. W., Lowe, A. G., Richter, A., et al. (2002). Antarctic springtime depletion of atmospheric mercury. *Environmental Science & Technology*, *36*, 1238–1244. https://doi.org/10.1021/es015710z

Fan, S-M, & Jacob, D. J. (1992). Surface ozone depletion in Arctic spring sustained by bromine reactions on aerosols. *Nature*, *359*, 522–524. https://doi.org/10.1038/359522a0

Frieß, U., Sihler, H., Sander, R., PöHler, D., Yilmaz, S., & Platt, U. (2011). The vertical distribution of BrO and aerosols in the Arctic: Measurements by active and passive differential optical absorption spectroscopy. *Journal of Geophysical Research*, *116*, D00R04. https://doi.org/10.1029/2011JD015938

Graham, R. M., Cohen, L., Petty, A. A., Boisvert, L. N., Rinke, A., Hudson, S. R., et al. (2017). Increasing frequency and duration of Arctic winter warming events. *Geophysical Research Letters*, *44*, 6974–6983. https://doi.org/10.1002/2017GL073395

Greenblatt, G. D., Orlando, J. J., Burkholder, J. B., & Ravishankara, A. R. (1990). Absorption measurements of oxygen between 330 and 1140 nm. *Journal of Geophysical Research*, *95*(D11), 18,557–18,582.

Hausmann, M., & Platt, U. (1994). Spectroscopic measurement of bromine oxide and ozone in the high Arctic during Polar Sunrise Experiment 1992. *Journal of Geophysical Research*, *99*(D12), 25,399–25,413.

Hegels, E., Crutzen, P. J., Klupfel, T., Perner, D., & Burrows, J. P. (1998). Global distribution of atmospheric bromine-monoxide from GOME on Earth Observing Satellite ERS-2. *Geophysical Research Letters*, *25*(16), 3127–3130.

Hendrick, F., Rozanov, A., Johnston, P. V., Bovensmann, H., De Mazière, M., Fayt, C., et al. (2009). Multi-year comparison of stratospheric BrO vertical profiles retrieved from SCIAMACHY limb and ground-based UV-visible measurements. *Atmospheric Measurement Techniques*, *1*, 273–285.

Hendrick, F., Van Roozendael, M., Chipperfield, M. P., Dorf, M., Goutail, F., Yang, X., et al. (2007). Retrieval of stratospheric and tropospheric BrO profiles and columns using ground-based zenith-sky DOAS observations at Harestua, 60°N. *Atmospheric Chemical Physics*, *7*, 4869–4885. https://doi.org/10.5194/acp-7-4869-2007

Hollwedel, J., Wenig, M., Beirle, S., Kraus, S., KÃijhl, S., Wilms-Grabe, W., et al. (2004). Year-to-year variations of spring time polar tropospheric BrO as seen by GOME. *Advances in Space Research*, *34*(4), 804–808.

Holmes, C. D., Jacob, D. J., Corbitt, E. S., Mao, J., Yang, X., Talbot, R., & Slemr, F. (2010). Global atmospheric model for mercury including oxidation by bromine atoms. *Atmospheric Measurement Techniques*, *10*, 12,037–12,057. https://doi.org/10.5194/acp-10-12037-2010

Holmes, C. D., Jacob, D. J., Corbitt, E. S., & Yang, X. (2006). Global lifetime of elemental mercury against oxidation by bromine in the free troposphere. *Geophysical Research Letters*, *33*, L20808. https://doi.org/10.1029/2006GL027176

Hönninger, G., Leser, H., Sebastián, O., & Platt, U. (2004). Ground-based measurements of halogen oxides at the Hudson Bay by longpath DOAS and passive MAX-DOAS. *Geophysical Research Letters*, *31*, L04111. https://doi.org/10.1029/2003GL018982

Hönninger, G., & Platt, U. (2002). Observations of BrO and its vertical distribution during surface ozone depletion at Alert. *Atmospheric Environment*, *36*, 2481–2489.

Jacobi, H. W., Voisin, D., Jaffrezo, J. L., Cozic, J., & Douglas, T. A. (2012). Chemical composition of the snowpack during the OASIS spring campaign 2009 at Barrow, Alaska. *Journal of Geophysical Research*, *117*, D00R13. https://doi.org/10.1029/2011JD016654

Jones, A. E., Anderson, P. S., Begoin, M., Brough, N., Hutterli, M. A., Marshall, G. J., et al. (2009). BrO, blizzards, and drivers of polar tropospheric ozone depletion events. *Atmospheric Chemical Physics*, *9*, 4639–4652. https://doi.org/10.5194/acp-9-4639-2009

Jones, A. E., Anderson, P. S., Wolff, E. W., Roscoe, H. K., Marshall, G. J., Richter, A., et al. (2010). Vertical structure of Antarctic tropospheric ozone depletion events: Characteristics and broader implications. *Atmospheric Chemical Physics*, *10*, 7775–7794. https://doi.org/10.5194/acp-10-7775-2010

Jones, A. E., Anderson, P. S., Wolff, E. W., Turner, J., Rankin, A. M., & Colwell, S. R. (2006). A role for newly forming sea ice in springtime polar tropospheric ozone loss? Observational evidence from Halley station, Antarctica. *Journal of Geophysical Research*, *111*, D08306. https://doi.org/10.1029/2005JD006566

Jones, A. E., Weller, R., Anderson, P. S., Jacobi, H.-W., Wolff, E. W., Schrems, O., & Miller, H. (2001). Measurements of NO_x, emissions from the Antarctic snowpack. *Geophysical Research Letters*, *28*, 1499–1502.

Kaleschke, L., Richter, A., Burrows, J. P., Afe, O., Heygster, G., Notholt, J., et al. (2004). Frost flowers on sea ice as a source of sea salt and their influence on tropospheric halogen chemistry. *Geophysical Research Letters*, *31*, L16114. https://doi.org/10.1029/2004GL020655

Krnavek, L., Simpson, W. R., Carlson, D., Domine, F., Douglas, T. A., & Sturm, M. (2012). The chemical composition of surface snow in the Arctic: Examining marine, terrestrial, and atmospheric influences. *Atmospheric Environment*, *50*, 349–359. https://doi.org/10.1016/j.atmosenv.2011.11.033

Kurosu, T. P., & Chance, K. (2011). OMBRO Readme file. Retrieved from http://www.cfa.harvard.edu/~tkurosu/SatelliteInstrume-nts/OMI/PGEReleases/index.html

Leck, C., Norman, M., Bigg, E. K., & Hillamo, R. (2002). Chemical composition and sources of the high Arctic aerosol relevant for cloud formation. *Journal of Geophysical Research*, *107*(D12), 4135. https://doi.org/10.1029/2001JD001463

Levelt, P., Joiner, J., Tamminen, J., Veefkind, P., Bhartia, P. K., Stein Zweers, D., et al. (2017). The Ozone Monitoring Instrument. https://doi.org/10.5194/acp-2017-487

Levelt, P. F., van den Oord, G. H. J., Dobber, M. R., Mälkki, A., Visser, H., de Vries, J., et al. (2006). The Ozone Monitoring Instrument. *IEEE Transactions on Geoscience and Remote Sensing*, *44*(5), 1093–1101. https://doi.org/10.1109/TGRS.2006.872333

Liao, J., Huey, L. G., Tanner, D. J., Flocke, F. M., Orlando, J. J., Neuman, J. A., et al. (2012). Observations of inorganic bromine (HOBr, BrO, and Br2) speciation at Barrow, AK, in spring 2009. *Journal of Geophysical Research*, *117*, D00R16. https://doi.org/10.1029/2011JD016641

Liao, J. L. G., Huey, L. G., Scheuer, E., Dibb, J. E., Stickel, R. E., Tanner, D. J., et al. (2012). Characterization of soluble bromide measurements and a case study of BrO observations during ARCTAS. *Atmospheric Chemical Physics*, *12*, 1327–1338. https://doi.org/10.5194/acp-12-1327-2012

Liao, J., Sihler, H., Huey, L. G., Neuman, J. A., Tanner, D. J., Friess, U., et al. (2011). A comparison of Arctic BrO measurements by chemical ionization mass spectrometry and long path-differential optical absorption spectroscopy. *Journal of Geophysical Research*, *116*, D00R02. https://doi.org/10.1029/2010JD014788

Lieb-Lappen, R. M., & Obbard, R. W. (2015). The role of blowing snow in the activation of bromine over first-year Antarctic sea ice. *Atmospheric Chemical Physics*, *15*, 7537–7545. https://doi.org/10.5194/acp-15-7537-2015

Lu, J. Y., Schroeder, W. H., Barrie, L. A., Steffen, A., Welch, H. E., Martin, K., et al. (2001). Magnification of atmospheric mercury deposition to polar regions in springtime: The link to tropospheric ozone depletion chemistry. *Geophysical Research Letters*, *28*, 3219–3222. https://doi.org/10.1029/2000GL012603

Malicet, J., Daumont, D., Charbonnier, J., Parisse, C., Chakir, A., & Brion, J. (1995). Ozone UV spectroscopy. II. Absorption cross-sections and temperature dependence. *Journal of Atmospheric Chemistry*, *21*, 263–273. https://doi.org/10.1007/BF00696758

Mann, G. W., Anderson, P. S., & Mobbs, S. D. (2000). Profile measurements of blowing snow at Halley, Antarctica. *Journal of Geophysical Research*, *105*(D19), 24,491–24,508. https://doi.org/10.1029/2000JD900247

Manney, G. L., Santee1, M. L., Rex, M., Livesey, N. J., Pitts, M. C., Veefkind, P., et al. (2011). Unprecedented Arctic ozone loss in 2011. *Nature*, *478*, 469–475. https://doi.org/10.1038/nature10556

Martinez, M., Arnold, T., & Perner, D. (1999). The role of bromine and chlorine chemistry for arctic ozone depletion events in Ny-Alesund and comparison with model calculations. *Annales Geophysicae*, *17*, 941–956.

Maslanik, J. A., Fowler, C., Stroeve, J., Drobot, S., Zwally, J., Yi, D., & Emery, W. (2007). A younger, thinner Arctic ice cover: Increase potential for rapid, extensive sea-ice loss. *Geophysical Research Letters*, *34*, L24501. https://doi.org/10.1029/2007GL032043

Massom, R. A., Drinkwater, M. R., & Haas, C. (1997). Winter snow cover on sea ice in the Weddell Sea. *Journal of Geophysical Research*, *102*(C1), 1101–1117. https://doi.org/10.1029/96JC02992

Massom, R. A., Eicken, H., Hass, C., Jeffries, M. O., Drinkwater, M. R., Sturm, M., et al. (2001). Snow on Antarctic sea ice. *Reviews of Geophysics*, *39*, 413–445. https://doi.org/10.1029/2000RG000085

Massom, R. A., Lytle, V. I., Worby, A. P., & Allison, I. (1998). Winter snow cover variability on East Antarctic sea ice. *Journal of Geophysical Research*, *103*(Cll), 24,837–24,855. https://doi.org/10.1029/98JC01617

May, N. W., Quinn, P. K., McNamara, S. M., & Pratt, K. A. (2016). Multiyear study of the dependence of sea salt aerosol on wind speed and sea ice conditions in the coastal Arctic. *Journal of Geophysical Research: Atmospheres*, *121*, 9208–9219. https://doi.org/10.1002/2016JD025273

McElroy, C. T., McLinden, C. A., & McConnell, J. C. (1999). Evidence for bromine monoxide in the free troposphere during the Arctic polar sunrise. *Nature*, *397*, 338–341. https://doi.org/10.1038/16904

McPeters, R., Kroon, M., Labow, G., Brinksma, E., Balis, D., Petropavlovskikh, I., et al. (2008). Validation of the Aura Ozone Monitoring Instrument total column ozone product. *Journal of Geophysical Research*, *113*, D15S14. https://doi.org/10.1029/2007JD008802

Neuman, J. A., Nowak, J. B., Huey, L. G., Burkholder, J. B., Dibb, J. E., Holloway, J. S., et al. (2010). Bromine measurements in ozone depleted air over the Arctic Ocean. *Atmospheric Chemical Physics*, *10*, 6503–6514. Retrieved from http://www.atmos-chem-phys.net/10/6503/2010/

Nghiem, S. V., Rigor, I. G., Perovich, D. K., Clemente-Colón, P., Weatherly, J. W., & Neumann, G. (2007). Rapid reduction of Arctic perennial sea ice. *Geophysical Research Letters*, *34*, L19504. https://doi.org/10.1029/2007GL031138

Nghiem, S. V., Rigor, I. G., Richter, A., Burrows, J. P., Shepson, P. B., Bottenheim, J., et al. (2012). Field and satellite observations of the formation and distribution of Arctic atmospheric bromine above a rejuvenated sea ice cover. *Journal of Geophysical Research*, *117*, D00S05. https://doi.org/10.1019.2011JD016268

Palm, S. P., Yang, Y., Spinhirne, J. D., & Marshak, A. (2011). Satellite remote sensing of blowing snow properties over Antarctica. *Journal of Geophysical Research*, *116*, D16123. https://doi.org/10.1029/2011JD015828

Parrella, J. P., Jacob, D. J., Liang, Q., Zhang, Y., Mickley, L. J., Miller, B., et al. (2012). Tropospheric bromine chemistry: Implications for present and pre-industrial ozone and mercury. *Atmospheric Chemistry and Physics*, *12*, 6723–6740. https://doi.org/10.5194/acp-12-6723-2012

Perovich, D. K., Richter-Menge, J., Jones, K. F., & Light, B. (2008). Sunlight, water, and ice: Extreme Arctic sea ice melt during summer 2007. *Geophysical Research Letters*, *35*, L11501. https://doi.org/10.1029/2008GL034007

Peterson, P. K., Pöhler, D., Sihler, H., Zielcke, J., General, S., Frieß, U., et al. (2017). Observations of bromine monoxide transport in the Arctic sustained on aerosol particles. *Atmospheric Chemical Physics*, *17*, 7567–7579. https://doi.org/10.5194/acp-17-7567-2017

Peterson, P. K., Simpson, W. R., Pratt, K. A., Shepson, P. B., Frieß, U., Zielcke, J., et al. (2015). Dependence of the vertical distribution of bromine monoxide in the lower troposphere on meteorological factors such as wind speed and stability. *Atmospheric Chemistry and Physics*, *15*, 2119–2137. https://doi.org/10.5194/acp-15-2119-2015

Pöhler, D., Vogel, L., Frieß, U., & Platt, U. (2010). Observation of halogen species in the Amundsen Gulf, Arctic, by active long-path differential optical absorption spectroscopy. *Proceedings of the National Academy of Sciences of the United States od America*, *107*, 6582–6587. https://doi.org/10.1073/pnas.0912231107

Prados-Roman, C., Butz, A., Deutschmann, T., Dorf, M., Kritten, L., Minikin, A., et al. (2011). Airborne DOAS limb measurements of tropospheric trace gas profiles: case studies on the profile retrieval of O_4 and BrO. *Atmospheric Measurement Techniques*, *4*, 1241–1260. https://doi.org/10.5194/amt-4-1241-2011

Pratt, K. A., Custard, K. D., Shepson, P. B., Douglas, T. A., Pöhler, D., General, S., et al. (2013). Photochemical production of molecular bromine in Arctic surface snowpacks. *Nature Geoscience*, *6*, 351–356. https://doi.org/10.1038/ngeo1779

Puķīte, J., Kühl, S., Deutschmann, T., Platt, U., & Wagner, T. (2010). Extending differential optical absorption spectroscopy for limb measurements in the UV. *Atmospheric Measurement Techniques*, *3*, 631–653.

Rhodes, R. H., Yang, X., Wolff, E. W., McConnell, J. R., & Frey, M. M. (2017). Sea ice as a source of sea salt aerosol to Greenland ice cores: A model-based study. *Atmospheric Chemical Physics*, *17*, 9417–9433. https://doi.org/10.5194/acp-17-9417-2017

Richter, A., Wittrock, F., Eisinger, M., & Burrows, J. P. (1998). GOME observations of tropospheric BrO in northern hemispheric spring and summer 1997. *Geophysical Research Letters*, *25*, 2683–2686. https://doi.org/10.1029/98GL52016

Richter-Menge, J., Comiso, J., Meier, W. N., Nghiem, S. V., & Perovich, D. (2008). Sea ice cover. *Bulletin of the American Meteorological Society*, *89*, S90–S91.

Rienecker, M. M., Suarez, M. J., Gelaro, G., Todling, R., Bacmeister, J., Liu, E., et al. (2011). MERRA: NASA's Modern-Era Retrospective Analysis for Research and Applications. *Journal of Climate*, *24*, 3624–3648. https://doi.org/10.1175/JCLI-D-11-00015.1

Rienecker, M. M., Suarez, M. J., Todling, R., Bacmeister, J., Takacs, L., Liu, H., et al. (2008). The GEOS-5 Data Assimilation System—Documentation of versions 5.0.1 and 5.1.0, and 5.2.0. NASA Tech. Rep. Series on Global Modeling and Data Assimilation, NASA/TM-1450 2008-104606.

Rinke, A., Maturilli, M., Graham, R. M., Matthes, H., Handorf, D., Cohen, L., et al. (2017). Extreme cyclone events in the Arctic. Wintertime variability and trends. *Environmental Research Letters*, *12*(9), 094006. https://doi.org/10.1088/1748-9326/aa7def

Saiz-Lopez, A., Lamarque, J.-F., Kinnison, D. E., Tilmes, S., Ordóñez, C., Orlando, J. J., et al. (2012). Estimating the climate significance of halogen-driven ozone loss in the tropical marine troposphere. *Atmospheric Chemical Physics*, *12*, 3939–3949. https://doi.org/10.5194/acp-12-3939-2012

Salawitch, R., Canty, T. P., Kurosu, T. P., Chance, K., Liang, Q., da Silva, A., et al. (2010). A new interpretation of total column BrO during Arctic spring. *Geophysical Research Letters*, *37*, L21805. https://doi.org/10.1029/2010GL043798

Schenkeveld, V. M. E., Jaross, G., Marchenko, S., Haffner, D., Kleipool, Q. L., Rozemeijer, N. C., et al. (2017). In-flight performance of the Ozone Monitoring Instrument. *Atmospheric Measurement Techniques*, *10*, 1957–1986. https://doi.org/10.5194/amt-10-1957-2017

Schmidt, R. A. (1982). Vertical profiles of wind speed, snow concentration, and humidity in blowing snow. *Boundary-Layer Meteorology*, *23*, 223–246. https://doi.org/10.1007/BF00123299

Schofield, R., Johnston, P. V., Thomas, A., Kreher, K., Connor, B. J., Wood, S., et al. (2006). Tropospheric and stratospheric BrO columns over arrival heights, Antarctica, 2002. *Journal of Geophysical Research*, *111*, D22310. https://doi.org/10.1029/2005JD007022

Seigneur, C., & Lohman, K. (2008). Effect of bromine chemistry on the atmospheric mercury cycle. *Journal of Geophysical Research*, *113*, D23309. https://doi.org/10.1029/2008JD010262

Serreze, M. C., Maslanik, J. A., & Key, J. R. (1997). Atmospheric and sea ice characteristics of the Arctic Ocean and the SHEBA field region in the Beaufort Sea (Vol. 4), National Snow and Ice Data Center, Cooperative Institute for Research in Environmental Sciences.

Sihler, H., Platt, U., Beirle, S., Marbach, T., Kühl, S., Dörner, S., et al. (2012). Tropospheric BrO column densities in the Arctic derived from satellite: Retrieval and comparison to ground-based measurements. *Atmospheric Measurement Techniques*, *5*, 2779–2807. https://doi.org/10.5194/amt-5-2779-2012

Simpson, W. R., Carlson, D., Hönninger, G., Douglas, T. A., Sturm, M., Perovich, D., & Platt, U. (2007). First-year sea-ice contact predicts bromine monoxide (BrO) levels at Barrow, Alaska better than potential frost flower contact. *Atmospheric Chemical Physics*, *7*, 621–627. https://doi.org/10.5194/acp-7-621-2007

Simpson, W. R., Peterson, P. K., Frieß, U., Sihler, H., Lampel, J., Platt, U., et al. (2017). Horizontal and vertical structure of reactive bromine events probed by bromine monoxide MAX-DOAS. *Atmospheric Chemical Physics*, *17*, 9291–9309. https://doi.org/10.5194/acp-17-9291-2017

Simpson, W. R., von Glasow, R., Riedel, K., Anderson, P., Ariya, P., Bottenheim, J., et al. (2007). Halogens and their role in polar boundary-layer ozone depletion. *Atmospheric Chemical Physics*, *7*, 4375–4418. https://doi.org/10.5194/acp-7-4375-2007

Spurr, R. J. D., Kurosu, T. P., & Chance, K. (2001). A linearized discrete ordinate radiative transfer model for atmospheric remote sensing retrieval. *Journal of Quantitative Spectroscopy and Radiative Transfer*, *68*, 689–735. https://doi.org/10.1016/S0022-4073(00)00055-8

Steffen, A., Bottenheim, J., Cole, A., Douglas, T. A., Ebinghaus, R., Friess, U., et al. (2013). Atmospheric mercury over sea ice during the OASIS-2009 campaign. *Atmospheric Chemical Physics*, *13*, 7007–7021. https://doi.org/10.5194/acp-13-7007-2013

Strahan, S. E., Duncan, B. N., & Hoor, P. (2007). Observationally derived transport diagnostics for the lowermost stratosphere and their application to the GMI chemistry and transport model. *Atmospheric Chemical Physics*, *7*, 2435–2445. https://doi.org/10.5194/acp-7-2435-2007

Suleiman, R. M., Chance, K., Liu, X., González Abad, G., Kurosu, T. P., Hendrick, F., & Theys, N. (2018). OMI total bromine monoxide (OMBRO) data product: Algorithm, retrieval and measurement comparisons. *Atmospheric Measurement Techniques Discuss.* https://doi.org/10.5194/amt-2018-1

Sumner, A. L., & Shepson, P. B. (1999). Snowpack production of formaldehyde and its effect on the Arctic troposphere. *Nature*, *398*, 230–233. https://doi.org/10.1038/18423

Theys, N., De Smedt, I., Van Roozendael, M., Fayt, C., Chabrillat, S., Chipperfield, M., et al. (2004). Total and tropospheric BrO derived from GOME and SCIAMACHY as part of TEMIS project. In *Envisat/ERS Symposium*. Salzburg.

Theys, N., Van Roozendael, M., Errera, Q., Hendrick, F., Dareden, F., Chabrillat, S., et al. (2009). A global stratospheric bromine monoxide climatology based on BASCOE chemical transport model. *Atmospheric Chemical Physics*, *9*, 831–848. https://doi.org/10.5194/acp-9-831-2009

Theys, N., Van Roozendael, M., Hendrick, F., Yang, X., De Smedt, I., Richter, A., et al. (2011). Global observation of tropospheric BrO column using GOME-2 satellite data. *Atmospheric Chemical Physics*, *11*, 1791–1811. https://doi.org/10.5194/acp-11-1791-2011

Toom-Sauntry, D., & Barrie, L. A. (2002). Chemical composition of snowfall in the high Arctic: 1990–1994. *Atmospheric Environment*, *36*(15-16), 2683–2693. https://doi.org/10.1016/S1352-2310(02)00115-2

Toumi, R. (1994). BrO as a sink for dimethylsulphide in the marine atmosphere. *Geophysical Research Letters*, *21*(2), 117–120. https://doi.org/10.1029/93GL03536

Toyota, K., McConnell, J. C., Lupu, A., Neary, L., McLinden, C. A., Richter, A., et al. (2011). Analysis of reactive bromine production and ozone depletion in the Arctic boundary layer using 3-D simulations with GEM-AQ: Inference from synoptic-scale patterns. *Atmospheric Chemical Physics*, *11*, 3949–3979. https://doi.org/10.5194/acp-11-3949-2011

Toyota, K., McConnell, J. C., Staebler, R. M., & Dastoor, A. P. (2014). Air-snowpack exchange of bromine, ozone and mercury in the springtime Arctic simulated by the 1-D model PHANTAS — Part 1: In-snow bromine activation and its impact on ozone. *Atmospheric Chemical Physics*, *14*, 4101–4133. https://doi.org/10.5194/acp-14-4101-2014

Tschudi, M., Fowler, C., Maslanik, J., Stewart, J. S., & Meier, W. (2017). EASE-Grid Sea Ice Age, Version 3, NASA National Snow and Ice Data Center Distributed Active Archive Center, Boulder, CO. https://doi.org/10.5067/PFSVFZA9Y85G

Tuckermann, M., Ackermann, R., Golz, C., Lorenzen-Schmidt, H., Senne, R., Stutz, J., et al. (1997). DOAS-observation of halogen radical-catalysed Arctic boundary layer ozone destruction during the ARCTOC-campaigns 1995 and 1996 in Ny-Alesund, Spitsbergen. *Tellus*, *49B*, 533–555.

Van Roozendael, M., Wagner, T., Richter, A., Pundt, I., Arlander, D. W., Burrows, J. P., et al. (2002). Intercomparison of BrO measurements from ERS-2 GOME, ground-based and balloon platforms. *Advances in Space Research*, *29*(11). https://doi.org/10.1016/S0273-1177(02)00098-4

Vasilkov, A. P., Joiner, J., Spurr, R. J. D., Bhartia, P. K., Levelt, P. F., & Stephens, G. (2008). Evaluation of the OMI cloud pressures derived from rotational Raman scattering by comparisons with other satellite data and radiative transfer simulations. *Journal of Geophysical Research*, *113*, D15S19. https://doi.org/10.1029/2007JD008689

von Glasow, R., & Crutzen, P. J. (2004). Model study of multiphase DMS oxidation with a focus on halogens. *Atmospheric Chemical Physics*, *4*, 589–608. https://doi.org/10.5194/acp-4-589-2004

Wagner, T., Ibrahim, O., Sinreich, R., Frieß, U., von Glasow, R., & Platt, U. (2007). Enhanced tropospheric BrO concentrations over Antarctic sea ice in mid winter observed from MAX-DOAS on board the research vessel Polarstern. *Atmospheric Chemistry and Physics*, *7*, 3129–3142. https://doi.org/10.5194/acp-7-3129-2007

Wagner, T., & Platt, U. (1998). Satellite mapping of enhanced BrO concentrations in the troposphere. *Nature*, *395*, 486–490. https://doi.org/10.1038/26723

Wennberg, P. (1999). Bromine explosion. *Nature*, *397*, 299–300.

Willmes, S, & Heinemann, G. (2015). Sea-ice wintertime lead frequencies and regional characteristics in the Arctic, 2003–2015. *Remote Sensing*, *8*(1), 4. https://doi.org/10.3390/rs8010004

Wilmouth, D. M., Hanisco, T. F., Donahue, N. M., & Anderson, J. G. (1999). Fourier transform ultraviolet spectroscopy of the A (2)Pi(3/2) <- X (II3/2)-I-2 transition of BrO. *The Journal of Physical Chemistry A*, *103*, 8935–8945. https://doi.org/10.1021/jp991651o

Winker, D. M., Hunt, W. H., & McGill, M. J. (2007). Initial performance assessment of CALIOP. *Geophysical Research Letters*, *34*, L19803. https://doi.org/10.1029/2007GL030135

Winker, D. M., Vaughan, M. A., Omar, A., Hu, Y., Powell, K. A., Liu, Z., et al. (2009). Overview of the CALIPSO mission and CALIOP data processing algorithms. *Journal of Atmospheric and Oceanic Technology*, *26*, 2310–2323. https://doi.org/10.1175/2009JTECHA1281.1

Wren, S. N., Donaldson, D. J., & Abbatt, J. P. D. (2013). Photochemical chlorine and bromine activation from artificial saline snow. *Atmospheric Chemical Physics*, *13*, 9789–9800. https://doi.org/10.5194/acp-13-9789-2013

Yang, X., Cox, R. A., Warwick, N. J., Pyle, J. A., Carver, G. D., O'Connor, F. M., & Savage, N. H. (2005). Tropospheric bromine chemistry and its impacts on ozone: A model study. *Journal of Geophysical Research*, *110*, D23311. https://doi.org/10.1029/2005JD006244

Yang, X., Pyle, J. A., & Cox, R. A. (2008). Sea salt aerosol production and bromine release: Role of snow on sea ice. *Geophysical Research Letters*, *35*, L16815. https://doi.org/10.1029/2008GL034536

Yang, X., Pyle, J. A., Cox, R. A., Theys, N., & Van Roozendael, M. (2010). Snow-sourced bromine and its implications for polar tropospheric ozone. *Atmospheric Chemical Physics*, *10*, 7763–7773. https://doi.org/10.5194/acp-10-7763-2010

Zhao, X., Strong, K., Adams, C., Schofield, R., Yang, X., Richter, A., et al. (2016). A case study of a transported bromine explosion event in the Canadian High Arctic. *Journal of Geophysical Research: Atmospheres*, *120*, 457–477. https://doi.org/10.1002/2015JD023711

Zhou, X., Beine, H. J., Honrath, R. E., Fuentes, J. D., Simpson, W. R., Shepson, P. B., & Bottenheim, J. W. (2001). Snowpack photochemical production of HONO: A major source of OH in the Arctic boundary layer in springtime. *Geophysical Research Letters*, *28*(21), 4087–4090. https://doi.org/10.1029/2001GL013531